Monthly Notices
of the
ROYAL ASTRONOMICAL SOCIETY

MNRAS **461,** 519–541 (2016) doi:10.1093/mnras/stw1260
Advance Access publication 2016 May 26

Physical properties of star clusters in the outer LMC as observed by the DES

A. Pieres,[1,2★] B. Santiago,[1,2★] E. Balbinot,[3★] E. Luque,[1,2] A. Queiroz,[1,2] L. N. da Costa,[2,4] M. A. G. Maia,[2,4] A. Drlica-Wagner,[5] A. Roodman,[6,7] T. M. C. Abbott,[8] S. Allam,[5] A. Benoit-Lévy,[9,10,11] E. Bertin,[9,11] D. Brooks,[10] E. Buckley-Geer,[5] D. L. Burke,[6,7] A. Carnero Rosell,[2,4] M. Carrasco Kind,[12,13] J. Carretero,[14,15] C. E. Cunha,[6] S. Desai,[16,17] H. T. Diehl,[5] T. F. Eifler,[18] D. A. Finley,[5] B. Flaugher,[5] P. Fosalba,[14] J. Frieman,[5,6] D. W. Gerdes,[19] D. Gruen,[6,7] R. A. Gruendl,[12,13] G. Gutierrez,[5] K. Honscheid,[20,21] D. J. James,[8] K. Kuehn,[22] N. Kuropatkin,[5] O. Lahav,[10] T. S. Li,[23] J. L. Marshall,[23] P. Martini,[20,24] C. J. Miller,[19,25] R. Miquel,[15,26] R. C. Nichol,[27] B. Nord,[5] R. Ogando,[2,4] A. A. Plazas,[18] A. K. Romer,[28] E. Sanchez,[29] V. Scarpine,[5] M. Schubnell,[19] I. Sevilla-Noarbe,[29] R. C. Smith,[8] M. Soares-Santos,[5] F. Sobreira,[2,30] E. Suchyta,[31] M. E. C. Swanson,[13] G. Tarle,[19] J. Thaler,[32] D. Thomas,[27] D. L. Tucker[5] and A. R. Walker[8]

Affiliations are listed at the end of the paper

Accepted 2016 May 23. Received 2016 May 23; in original form 2015 November 26

ABSTRACT

The Large Magellanic Cloud (LMC) harbours a rich and diverse system of star clusters, whose ages, chemical abundances and positions provide information about the LMC history of star formation. We use Science Verification imaging data from the Dark Energy Survey (DES) to increase the census of known star clusters in the outer LMC and to derive physical parameters for a large sample of such objects using a spatially and photometrically homogeneous data set. Our sample contains 255 visually identified cluster candidates, of which 109 were not listed in any previous catalogue. We quantify the crowding effect for the stellar sample produced by the DES Data Management pipeline and conclude that the stellar completeness is <10 per cent inside typical LMC cluster cores. We therefore reanalysed the DES co-add images around each candidate cluster and remeasured positions and magnitudes for their stars. We also implement a maximum-likelihood method to fit individual density profiles and colour–magnitude diagrams. For 117 (from a total of 255) of the cluster candidates (28 uncatalogued clusters), we obtain reliable ages, metallicities, distance moduli and structural parameters, confirming their nature as physical systems. The distribution of cluster metallicities shows a radial dependence, with no clusters more metal rich than [Fe/H] $\simeq -0.7$ beyond 8 kpc from the LMC centre. The age distribution has two peaks at $\simeq$1.2 and $\simeq$2.7 Gyr.

Key words: methods: statistical – Magellanic Cloud – galaxies: star clusters: general.

1 INTRODUCTION

The Large Magellanic Cloud (LMC) is a nearby dynamically active satellite galaxy, exhibiting multiple epochs of star formation, while also suffering from tidal interactions with the Small Magellanic Cloud (SMC) and the Milky Way (MW). Given its proximity, stellar populations in the LMC are easily resolved in deep surveys, allowing us to obtain information such as ages, chemical abundances, kinematics and distances to individual stars and star clusters. Thus, the LMC represents an excellent local laboratory to study the effects of gravitational forces on the evolution of a satellite galaxy,

---

★ E-mail: adriano.pieres@ufrgs.br (AP); basilio.santiago@ufrgs.br (BS); e.balbinot@surrey.ac.uk (EB)

Published by Oxford University Press on behalf of the Royal Astronomical Society

including its star formation history (SFH) and age–metallicity relation (AMR).

A wealth of data describing the structure and stellar populations of the LMC has been accumulated over decades of research. The LMC is known to have a stellar disc inclined relative to the line of sight towards its centre by $i = 36\text{–}38^\circ$ with a position angle of $\theta = 130\text{–}145^\circ$. This disc also seems to have a warp and to be flared (Caldwell & Coulson 1986; Alves & Nelson 2000; Olsen & Salyk 2002; Subramanian & Subramaniam 2010; Balbinot et al. 2015). A large number of studies have tried to reconstruct its SFH and/or AMR, often in connection to the SMC (Carrera et al. 2008, 2011; Harris & Zaritsky 2009; Glatt, Grebel & Koch 2010; Indu & Subramaniam 2011; Rubele et al. 2012; Piatti & Geisler 2013; Weisz et al. 2013; Meschin et al. 2014).

Regarding the stellar populations and their variation as a function of position, many studies attempt to reconstruct the SFH and/or AMR of the LMC, based on field stars (Carrera et al. 2008, 2011; Meschin et al. 2014), clusters in the relatively central region (<10 kpc) (Olszewski et al. 1991; Kontizas, Kontizas & Michalitsianos 1993; Geisler et al. 1997, 2007; Kerber, Santiago & Brocato 2007; Glatt, Grebel & Koch 2010) or both (Piatti & Geisler 2013). The results have been inconsistent, as no single SFH and AMR applies to the entire LMC body or to clusters and field stars alike (Carrera et al. 2011; Piatti & Geisler 2013). In a recent paper, Piatti & Geisler (2013) analyse 5.5 million LMC field stars and present age and metallicity trends with distance from the LMC centre (out to 8 kpc) and an AMR. Their results are more consistent with outside-in star formation and chemical enrichment. They also find larger spreads in age and metallicity in the outer regions and no clear age gap in the field star formation. Carrera et al. (2011) investigate fields stars farther out, from 5.2 to 9.2 kpc from the LMC centre, and find age and metallicity gradients only for the youngest and the most metal-rich stars. For the star clusters, Glatt et al. (2010) fit Padova (Girardi et al. 2002) and Geneva (Lejeune & Schaerer 2001) isochrones to a sample of 1193 young LMC clusters within 4 deg of its centre and find two periods of enhanced cluster formation, at 125 and 800 Myr. They argue that these peaks in the cluster formation rate may be connected with the last encounter of the LMC and SMC.

In contrast with our knowledge of the inner structure and stellar populations of the LMC, much less is known about the periphery at distances >10 kpc. Covering the extended outer LMC regions requires a large-area, photometric and homogeneous sample. This has recently been provided by the early data taken as part of the Dark Energy Survey (DES) Science Verification (SV). In this work we aim to probe clusters in the outer LMC field in DES-SV footprint, using a homogeneous data sample.

This paper is organized as follows: Section 2 is a brief introduction presenting the data (the DES-SV data set, its reduction and the resulting LMC clusters sample). Section 3 describes the methods we applied to recover cluster structural parameters and cluster stellar populations. In Section 4 we tested the limits of the methods, simulating clusters, recovery of parameters and determining uncertainties. Section 5 presents our results and compares to available literature. Section 6 provides a discussion and summary.

2 DATA

2.1 DES and SV

The DES (The Dark Energy Survey Collaboration 2005) is a 5000 deg^2 imaging survey in *grizY* bands currently being carried out using DECam, a 3 deg^2 (2°.2 diameter) wide-field mosaic camera on the CTIO Blanco 4 m telescope with a pixel scale of 0.263 arcsec pixel^{-1} (Flaugher et al. 2015). DES will reach a characteristic photometric depth of 24th magnitude (with S/N $\simeq$ 10 for g band, point-like sources) and enable accurate photometry and morphology of objects 10 times fainter than the Sloan Digital Sky Survey. The exposure times for DES single exposures are 90 s for *g, r, i, z* and 45 s for *Y* band.

The DECam images are reduced by the DES Data Management (DESDM) team, which has a pipeline to co-add and calibrate (astrometrically and photometrically) images and finally catalogue and classify the objects in the images. The final co-add images are called *tiles*, with a size of 0.75 deg × 0.75 deg ($10^4 \times 10^4$ pixels). More details can be found in Mohr et al. (2012) and Desai et al. (2012).

A substantial challenge for deep ground-based surveys is the star/galaxy separation. DESDM performs photometric analysis with SEXTRACTOR (Bertin & Arnouts 1996), a software package which identifies and selects sources above a threshold based on the image background. The blend parameter determines whether a group of neighbouring pixels must be classified as a single source or multiple objects (Bertin 2011). The final catalogue produces several magnitude measurements (*mag_auto* and *mag_psf*, for example) and *spread_model* as the main star/galaxy separator. This is based on the difference between the best-fitting local point spread function (PSF) model and a slightly more extended model made from the same PSF convolved with a circular exponential disc model with scalelength equal to FWHM/16 (where FWHM is the full width half-maximum of the PSF model).

The DES-SV data were taken from November 2012 to February 2013 for a total of 427 h of observation. The data were intended to test DECam capabilities and the DESDM data pipeline (calibration and photometry, astrometry, image quality, pointing and guiding, operational readiness and pipelines for supernova). The largest contiguous area of the SV campaign was the South Pole Telescope East field (SPT-E), which is located immediately to the north of the LMC. This work is based on the co-add data products from the first release processing of the SV observations (SVA1), which includes the SPT-E region (157 deg^2) in 2537 exposures.

2.2 LMC star clusters

An initial sample of LMC star clusters in the SPT-E region was obtained by a visual inspection of the SV co-add images [Red Giant Branch (RGB) images made co-added exposures in the g, r and i bands], on a tile by tile basis. We used the Tile Viewer tool available at the DES Science portal (Balbinot et al. 2012), which is a web-based facility. The list of SPT-E tiles was initially split among five of the authors with an overlap region among them. Almost all LMC clusters were found in the southern part of the field, which was inspected by two of us. The overlapping region included 10 clusters found by one of the authors, eight of which comprised the sample found by the other. Not unexpectedly, the two extra objects were poor clusters. Despite the low numbers, this sample overlap suggests a uniform sampling among the richer systems analysed in Section 5.2.

After eliminating repeats from the individual searches, the original cluster list contained 294 candidates. We then matched our candidates with the Bica et al. (2008) LMC clusters catalogue. Our list contains a total of 109 previously uncatalogued objects. Seven objects included in the Bica et al. (2008) catalogue were not in our original list. By visually inspecting their images, one of these objects was clearly a galaxy and another was very close to a bright star, leaving a total of 299 cluster candidates in the SPT-E region.

The sample was further refined using the g versus $g-r$ colour–magnitude diagrams (CMDs; from DAOPHOT, see Section 2.4). 44 out of the 299 visually inspected candidates had CMDs that were not consistent with simple or composite stellar populations, usually containing a large fraction of faint red sources, more consistent with galaxy clusters. The filtered subsample has 255 candidates consistent with being star clusters. The full list is available in VizieR database.

2.3 DES-SV stellar sample

Since the DES main goals are cosmological in nature, the science requirements for the data are related to detecting, measuring and characterizing galaxies, not stars. Therefore, we ran a complementary diagnostic of the DES-SV stellar catalogue. Our main concern was to investigate the completeness of the SVA1 stellar catalogue as a function of S/N and crowding, since this aspect is crucial to the analysis of LMC clusters presented here. For that purpose, we used routines from IRAF/DAOPHOT (Stetson 1987), which is the benchmark program to detect and measure stellar data in crowded fields. Details about our DAOPHOT reduction and photometry pipeline are provided in Section 2.4. A full description of stellar completeness in SVA1 catalogues can be found in a future technical paper (Pieres et al., in preparation). Below we summarize our basic conclusions:

(i) CMDs based on the stellar samples drawn from standard DAOPHOT selection, using PSF magnitude errors and sharpness, are similar to those from SVA1, based on *spread_model* cuts. In the SPT-E fields covering the outer LMC, the CMDs from both SVA1 and DAOPHOT clearly display the main features of the LMC field population, such as an Main Sequence (MS) ranging from $18 < g < 24$, an old Main Sequence Turnoff at $g{\sim}22.5$, $g-r \sim 0.2$, a red giant branch and a red clump with $g < 22$ and $g-r > 0.3$.

(ii) In typical DES regions, well away from the LMC, the source density is about 1/10 of that found in regions where most star clusters are found. In this low-density regime, as well as inside poor LMC clusters, SVA1 completeness relative to DAOPHOT is close to 1 down to $g \cong 20$. SVA1 catalogues tend to sample fewer point sources than DAOPHOT at fainter magnitudes, but the relative completeness varies depending on how we separate stars from galaxies in either case.

(iii) SVA1 stellar completeness is a strong function of source density, dropping abruptly from ${\sim}0.3$ to <0.1 for surface densities >260 stars arcmin^{-2}. In particular, the SVA1 stellar sample is very incomplete in crowded fields, such as those close to the centres of rich LMC star clusters. In these regions, SVA1 samples less than 50 per cent of the objects detected by DAOPHOT, even at bright magnitudes ($g < 19$). Inside rich cluster cores, the SVA1 incompleteness is large enough to cause local holes in the surface density distribution of point sources on the sky. This result is robust to the way we separate stars from galaxies.

With these results in mind, we decided that we could not use the SVA1 catalogues inside and around the LMC clusters. However, we used SVA1 co-add images to identify cluster candidates and its catalogs to fit zero-points to DAOPHOT photometry. We also decided to use three bands (two colours) instead of two, to better describe the stellar locus of each cluster candidate. For reference, a comparison of both software packages (SEXTRACTOR with PSFEX and DAOPHOT with ALLSTAR) can be found in Annunziatella et al. (2013). In Section 2.4 we describe in detail the data reduction and analysis based on our DAOPHOT pipeline.

2.4 DAOPHOT data reduction

As mentioned earlier, the SVA1 catalogue is incomplete in crowded regions, such as inside LMC star clusters. To bypass this problem, we used the SVA1 co-add image products in the vicinity of each of our candidate clusters as inputs for our own photometric extraction based on DAOPHOT. For each object we made an image cutout with 6.75 arcmin on a side, visually centred on the candidate, in three bands: g, r and i.

The IRAF/DAOPHOT routines were combined into a pipeline to reduce DES co-add cutouts (Fig. 1). This pipeline is a set of scripts using the tasks *daofind*, *phot*, *pstselect*, *psf*, *allstar* and works as follows. First, we combined g and r images and ran *daofind* to detect sources on these combined images; we rejected sources that were less than 3.0σ above the background. We then picked the 50 brightest sources to use as a starting template for PSF modelling (running *psf* task). With the initial PSF model, we ran *allstar* over all sources found and refined our initial list of stars used for PSF fitting by choosing those whose local background is ≤ 3 counts, and which have low magnitude error (≤ 0.01 mag) and low chi-square (≤ 0.2). This procedure of refining the PSF after an initial *allstar* run is meant to make the process subject to minimal human interference (although some human decisions were still needed at times). PYTHON and FORTRAN routines were made to select the stars and convert their α and δ coordinates to/from x and y coordinates. This conversion, whenever needed, uses the WCS of the DESDM co-adds, therefore preserving DESDM astrometry. The SVA1 catalogue has a typical accuracy of 200 mas per coordinate when compared to UCAC-4, and 100 mas for nearby sources. Using a program similar to the *join* Linux command, we then composed the DAOPHOT catalogues from each filter. We then added g, r and i zero-points, by taking DES catalogue photometry as reference, and created the final DAOPHOT catalogue. The stars used for this calibration were those that satisfied the following criteria: $magerr_{DAO} \leq 0.03$, $|sharp| \leq 1.00$ in g, r and i filters, brighter than 20 (in g and r filters) and 19 (for i *filter*). The corresponding sources in SVA1 had to have $|\ spread\_model\ | \leq 0.002$ and magnitude error ≤ 0.03. The standard deviation for these difference ($|mag_{DAO} - mag_{SVA1}|$) has typical values ≤ 0.02 for the three filters. This small random scatter after the zero-point correction precludes the need of adopting colour terms in the calibration.

After the reduction, diagnostic plots were made to evaluate the DAOPHOT catalogue completeness level and to make reduction sanity checks. An example of these diagnostic plots is shown in Fig. 2. Example $g \times [g-r]$ CMDs of clusters of different ages and richness are shown in Fig. 3. Details about parameters fitting are provided in Section 3.

The criteria we used to define sources as stars from the DAOPHOT catalogue were magnitude error ≤ 0.1 and |sharpness| ≤ 1.00 in g, r and i bands simultaneously. Stars used for refining the PSF model or for calibration purposes were subject to more stringent selection criteria, as explained earlier. Our DAOPHOT based selection of stars is still prone to substantial contamination by galaxies. However, within a typical visual cluster radius this contamination amounts to less than 2 per cent.

A parallel analysis of relative completeness (SVA1 and DAOPHOT catalogues, using the same pipeline reduction presented here) has been reported by Balbinot et al. (2015) in their section 3.3.

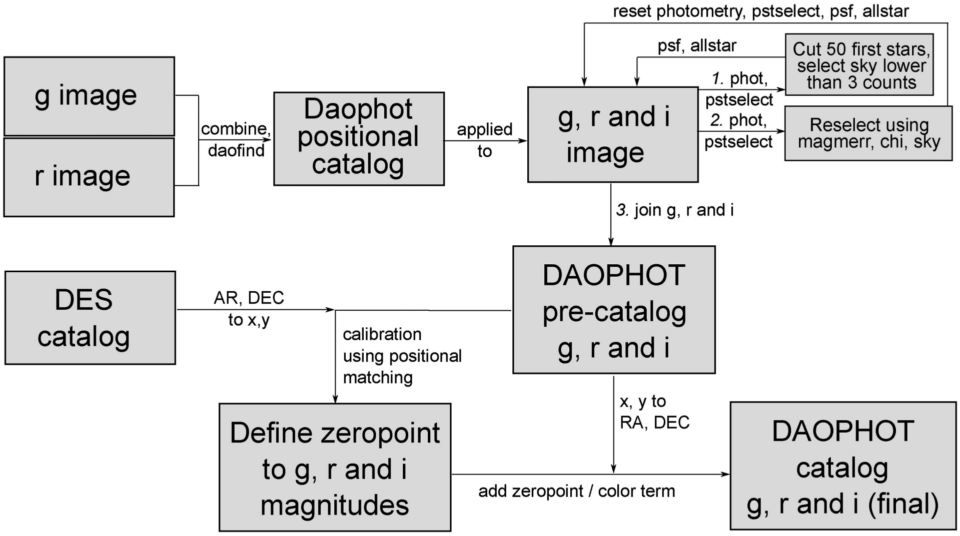

Figure 1. Flow chart describing the DAOPHOT based reduction and photometry pipeline developed as part of this work. As final products, it yields a catalogue using *g, r* and *i* magnitudes from co-add image cutouts. First, the *g* and *r* images are combined to generate a positional sources catalogue (using *daofind*). This catalogue is a starting point to run *phot* (for aperture measurements) and *pstselect* (for producing a list of stars to be used in the PSF model) routines for each filter. We pick the 50 brightest sources and run *psf* (that does the actual PSF modelling) and *allstar* (PSF fitting to all detected sources) tasks. A cleaner set of psf stars is selected as those sources with the lowest values of *chi, magerror, sky*, making up a new PSF list. We reset the list and rerun *psf* and *allstar*. The zero-point for each filter are determined comparing magnitudes of SVA1 (DESDM) and DAOPHOT after a positional match to the DES catalogue. Last, these calibration terms are added and the coordinates converted to α and δ, generating the final composite DAOPHOT catalogue.

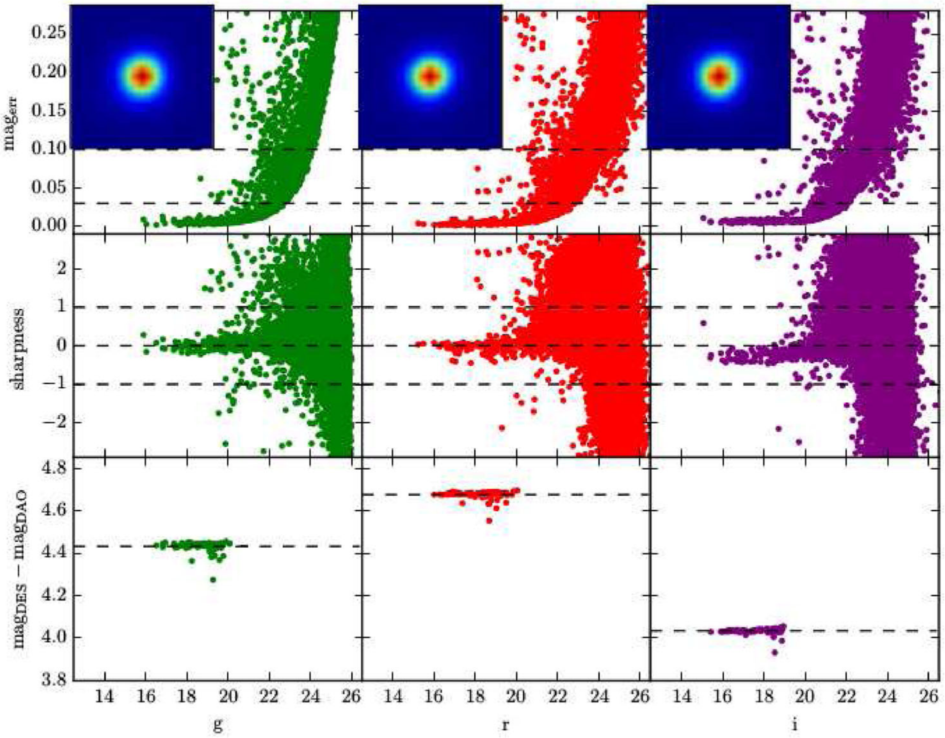

Figure 2. Diagnostic plot for the image reduction around our LMC cluster candidate 67. The three columns refer to *g*, *r* and *i* filters, from left to right. The upper row shows the DAOPHOT magnitude errors increasing towards fainter stars. The upper dashed line is the maximum magnitude error adopted to classify an object as a star. The lower dashed line is the cut-off used for calibration purposes. The model PSF images are shown at the top left of these panels. In the middle row, the sharpness parameter is plotted against the magnitudes. Again, the dashed lines limit the assumed stellar locus. The lower row shows the magnitude differences ($\mathrm{mag}_{\mathrm{DES}} - \mathrm{mag}_{\mathrm{DAO}}$) for classified stars that were used for calibration (the zero-point added to DAOPHOT was based in a mean of these stars). The outliers in the bottom panels were ruled out using a 3σ clipping algorithm.

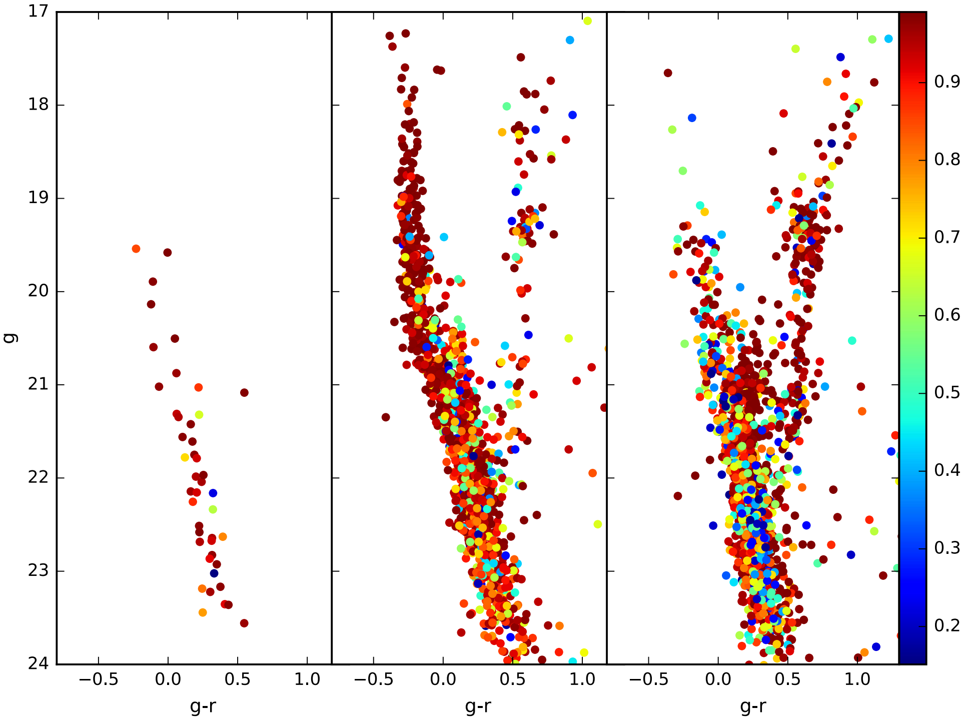

Figure 3. In order to illustrate the clusters richness in this sample, we show $g \times [g-r]$ CMDs for (leftmost panel) the poorest cluster in this sample (DES001SC17 with 44 stars and 1.26 Gyr as fitted age), the young (480 Myr) BSDL2976 cluster (central panel) and the intermediate-age (2.57 Gyr) SL388 cluster (rightmost panel). Stars are colour coded by their likelihood being cluster members assuming a King profile as described in equation (9).

3 METHODS

3.1 Radial density profiles

We used the King azimuthally symmetric profile (King 1962) as the standard model to describe the surface density profile of the star cluster candidates:

$$\rho_{\rm cl}(r) = k\left(\frac{1}{[1+(r/r_{\rm c})^2]^{1/2}} - \frac{1}{[1+(r_{\rm t}/r_{\rm c})^2]^{1/2}}\right)^2, \qquad (1)$$

where $\rho_{\rm cl}$ is the surface number density of cluster stars, r is the angular distance from the centre ($\alpha_{\rm c}$ and $\delta_{\rm c}$ in cutout), $r_{\rm c}$ is the cluster *core radius* and $r_{\rm t}$ is the cluster *tidal radius*. The parameter k is the profile normalization and is related to the central surface density. The King density profile is widely used for both high and low-mass Galactic clusters (Kharchenko et al. 2012; Miocchi et al. 2013).

The King parameters $r_{\rm c}$, $r_{\rm t}$ and centroid were determined using a maximum likelihood estimate (MLE). First, we determined the background density of stellar sources in the cutout image, $\rho_{\rm bg}$. We do that by counting stars farther than two times a visually determined cluster radius and dividing this number count by the corresponding area. After we determined the background density, we estimated the number of stars ($N_\star$) belonging to the cluster by following the recipe by Martin, de Jong & Rix (2008)

$$N_\star = N_{\rm tot} - \rho_{\rm bg} \times A, \qquad (2)$$

where A is the cutout area and $N_{\rm tot}$ is the total number of stars in the cutout. The profile normalization constant k is determined for each profile by dividing the number of cluster stars ($N_\star$) by the integral of the King profile from the centre to $r_{\rm t}$:

$$k = \frac{N_\star}{\int_0^{r_{\rm t}} 2\pi r\,{\rm d}r\left(\frac{1}{[1+(r/r_{\rm c})^2]^{1/2}} - \frac{1}{[1+(r_{\rm t}/r_{\rm c})^2]^{1/2}}\right)^2}. \qquad (3)$$

In the fitting process, we varied the centre position ($\alpha_{\rm c}$ and $\delta_{\rm c}$) and the parameters $r_{\rm c}$ and $r_{\rm t}$ (these parameters are determined from the model profile grid), evaluating the initial estimates by eye.

The likelihood that star i belongs to the full model (King profile) with radii $r_{\rm c}$ and $r_{\rm t}$ and centred at $\alpha_{\rm c}$ and $\delta_{\rm c}$ and normalized to k is

$$\ell_i = k\left(\frac{1}{[1+(r_i/r_{\rm c})^2]^{1/2}} - \frac{1}{[1+(r_{\rm t}/r_{\rm c})^2]^{1/2}}\right)^2 + \rho_{\rm bg}, \qquad (4)$$

where r_i is the radial distance of the given star from that model centre. The most likely model (defined by parameters $r_{\rm c}$, $r_{\rm t}$ and position $\alpha_{\rm c}$, $\delta_{\rm c}$) is the one which maximizes the log-likelihood summed over all stars:

$$\log \mathcal{L}(r_{\rm c}, r_{\rm t}, \alpha_{\rm c}, \delta_{\rm c}) = \sum_{i=1}^{N} \log(\ell_i), \qquad (5)$$

where N is $N_{\rm tot}$ in equation (2). Note that, in practice, stars located outside the tidal radius of each model profile contribute to the likelihood with $\ell_i = \rho_{\rm bg}$.

3.2 Isochrone fits

We also used a maximum-likelihood approach to determine the cluster simple stellar populations: age, metallicity, distance modulus and reddening. As in the fit for the density profiles, the basic step is to measure the likelihood that each star is taken from a modelled isochrone displaced by a given distance modulus and extinction vector. In this work, we are using three magnitudes, g, r and i. Thus, the distance from the isochrone in magnitude space must be evaluated in 3D space. For this purpose, we used the PARSEC isochrones (Bressan et al. 2012) and adopted the Galactic extinction law of Cardelli, Clayton & Mathis (1989). The reddening is used to constrain extinction as measured in each magnitude. As a result of our choice, extinction is then given as

$$A_g = 3.318E(g - r) \tag{6}$$

$$A_r = 2.318E(g - r) \tag{7}$$

$$A_i = 1.758E(g - r). \tag{8}$$

Note that this choice of extinction law leads to very similar results (within the uncertainties) to a typical LMC extinction curve (Gordon et al. 2003) for g, r and i DECam filters.

The isochrone fitting works as follows. Given the best-fitting density profile, we first assigned a probability that star i belongs to the candidate cluster as

$$P_i^{\rm kp} = \left(\frac{\rho_{\rm cl}(r_i)}{\rho_{\rm bg} + \rho_{\rm cl}(r_i)}\right), \tag{9}$$

where $\rho_{\rm bg}$ is the background star density, as described in the previous section. We applied a threshold cut in $P^{\rm kp} > 0.05$ to select the stars to use in the fit. We then computed the Gaussian likelihood that a given isochrone is the correct one describing this set of stars. We first determined the distance of star i to isochrone j, d_{ij}. This is the minimum distance of the star in the M-dimensional photometric space (in this case, g, r and i magnitudes) to the isochrone:

$$d_{ij}^2 = \min\left[\sum_{l=1}^{M}\left(\frac{m_{li} - m_{lj}}{\sigma_{m_{li}}}\right)^2\right], \tag{10}$$

where the sum is over all photometric bands, (m_{lj}) is the closest isochrone magnitude in band l to the observed magnitude of star i (m_{li}), and $\sigma_{m_{li}}$ is the uncertainty in m_{li}. The isochrone magnitudes are already displaced by the distance modulus and reddening, both of which are free fit parameters. To avoid numerical limitations, we interpolate the isochrone points when determining d_{ij}, instead of using the discrete set of isochrone points.

Note that d_{ij} corresponds to the highest likelihood term that the star i is drawn from isochrone model j, which is then given by

$$P_{ij} = \frac{1}{(2\pi)^{M/2}}\left(\prod_{l=1}^{M}\frac{1}{\sigma_{mli}}\right)\exp\left(\frac{-d_{ij}^2}{2}\right). \tag{11}$$

Finally, the logarithmic likelihood that the set of N stars that satisfies the $P^{\rm kp} > 0.05$ criterion are drawn from isochrone model j can be written as

$$\log \mathcal{L}_j = \log\prod_{i=1}^{N}(P_{ij}P_i^{\rm kp}) = \sum_{i=1}^{N}\log(P_{ij}) + \sum_{i=1}^{N}\log(P_i^{\rm kp}). \tag{12}$$

3.3 Optimization methods

We are dealing with a maximization problem where we want to find the model which best describes the set of likely cluster stars. Given a grid in parameter space of age, metallicity, distance and reddening, we found the peak of $\mathcal{L}$ ($\mathcal{L}_{\max}$), and we probe the $2\log(\mathcal{L})$ space around this global maximum. The $2\log(\mathcal{L})$ values behave similarly to a χ^2 distribution, assuming that uncertainties have Gaussian (or similar) behaviour close to the peak. In this way we estimate the $k\sigma$ confidence level in the same manner as the χ^2 distribution (Lupton 1993, section 10.3). The main difference is that we include the covariance among parameters using the profile likelihood technique (Fisher 1956; Sprott 2000). For example, when determining the uncertainty in the age we perform a likelihood scan where at each value of cluster age we maximizing the likelihood with respect to the other parameters. Thus, the $k\sigma$ confidence intervals are determined when the log of the profile likelihood drops by $(k^2)/2$ from its maximum value. The uncertainties quoted in this work correspond to 1σ confidence level (68 per cent).

In the cases where the quoted uncertainties are smaller than the half-bin size (as is the cases for a few metal-poor clusters), we take the error to be the maximum of the uncertainty as computed by the likelihood method and half of the bin size at the grid point corresponding to maximum likelihood. The uncertainties quoted here reflect the statistical uncertainty in the model fit, and do not include any systematic uncertainties in the derivation of synthetic isochrone models (e.g. Bressan et al. 2012).

We test our profile and isochrone fitting in simulated star clusters in Section 4. The next section presents the model grids to do that.

3.4 Model grids

The likelihood optimization methods outlined in the previous sections require a grid of models, both for the structure (profile fitting) and for the other physical parameters (CMD fitting).

The LMC clusters vary in size by about an order of magnitude, as will be shown later in this paper. Therefore, it was not possible to use a single grid in $r_{\rm c}$ and $r_{\rm t}$ for all clusters. Furthermore, initial guesses from visual estimates were not always useful in constraining an optimal range in core and tidal radii. As a result, the profile fits were carried out interactively, with a size grid that varied from one cluster to the other. The central positions were allowed to vary within $\pm r_{\rm t}/4$ as taken from the previous iteration, until convergence. We define convergence to occur when the algorithm indicates a likelihood maximum close to the centre of the parameter's range. For some candidates, the range in $r_{\rm t}$ continuously increased and reached the limit of the cutout (much greater than the visual radius), which means the set of stars does not present a clear overdensity. These cases were removed from our catalogue.

The CMD fits were carried out with a fixed initial set of isochrones from which we built a likelihood map for each cluster. This initial grid covers the range $8.12 \leq \log[\mathrm{age(yr)}] \leq 10.12$ with 10 equally spaced age steps of $\Delta\log[\mathrm{age(yr)}] = 0.2$. Metallicity varies within $0.0002 \leq Z \leq 0.019$ in 23 values: $0.0002 \leq Z \leq 0.0008$, step=0.0002; $0.001 \leq Z \leq 0.019$, step=0.001. The other dimensions are $18.2 \leq (m - M)_0 \leq 18.8$ with $\Delta(m - M)_0 = 0.03$ and $0 \leq E(g - r) \leq 0.2$ with $\Delta E(g - r) = 0.02$. This grid is the same for real and simulated clusters.

We scanned the entire initial grid, searching for a global likelihood maximum. We then defined another model grid around this maximum, which is narrower in log[age(yr)], covering $\log[\mathrm{age(yr)}]_{\max} - 0.4 \leq \log[\mathrm{age(yr)}] \leq \log[\mathrm{age(yr)}]_{\max} + 0.4$ with $\Delta\log[\mathrm{age(yr)}] = 0.02$, where $\log[\mathrm{age(yr)}]_{\max}$ is the age corresponding to the likelihood peak in the initial grid. Metallicity in this thinner grid was restricted to ±4 steps around the maximum likelihood value in the initial grid. Reddening and distance modulus were allowed to vary by ±0.05 and ±0.1, respectively, with 10 steps in each axis, from their initial best solution.

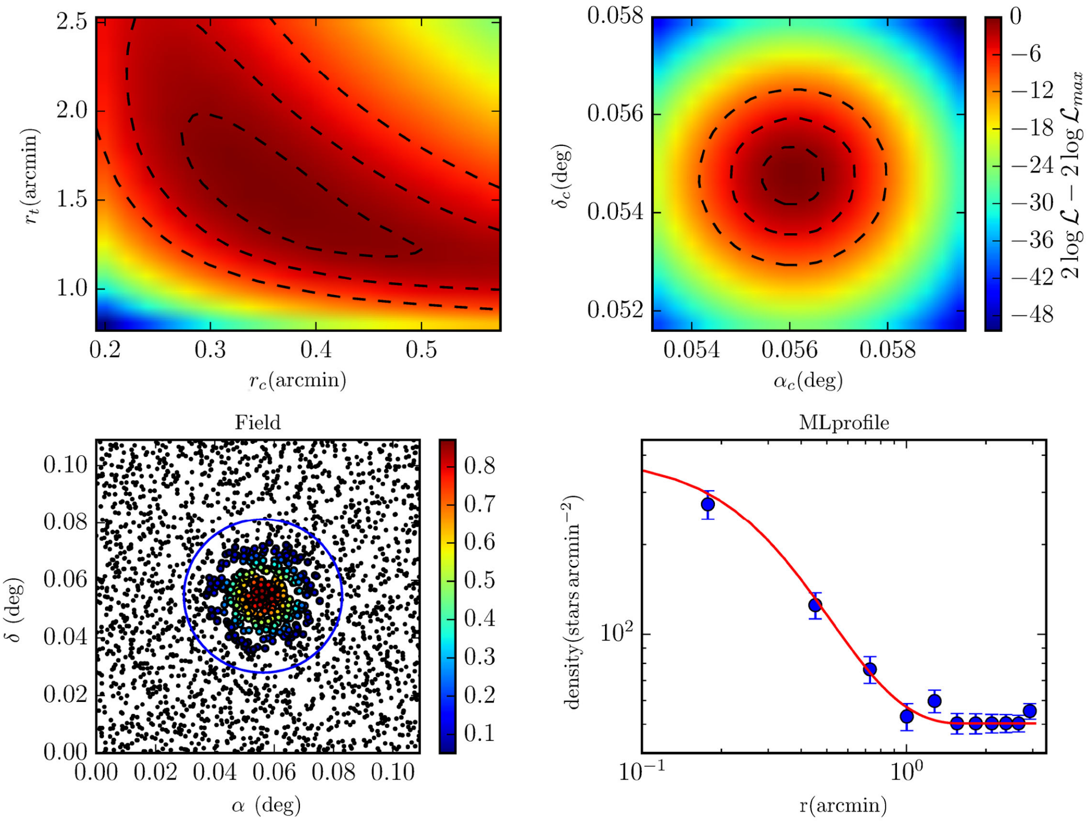

Figure 4. Example of the recovery of structural parameters for a simulated cluster (τ = 1Gyr and $Z = 0.010$). The most likely parameters (using the DECam plate scale = 0.263 arcsec pixel^{-1}) are $r_c = 0.33$ arcmin, $r_t = 1.60$ arcmin, $k = 536$ stars arcmin^{-2}. Top left: likelihood maps for grid in r_c and r_t. Top right: $2\log\mathcal{L}$ map for centre position (top-left and right-hand plots share same colour bar). Black dashed lines in both top panels show limits for 1σ, 2σ and 3σ confidence levels. Bottom left: on-sky distribution of stars, colour coded according to likelihood. Bottom right: binned profile (blue circles) and the best-fitting model profile (solid red line).

4 CLUSTER SIMULATIONS

We first tested the fitting methods for density profiles and isochrones described above using simulated data.

We built artificial star clusters using GENCMD[1] and we inserted the synthetic stars into a typical LMC field. This code generates simple stellar populations (α, δ, magnitudes and magnitudes errors) given an initial number of stars, a mass function, a spatial density profile, a set of isochrones, filters and typical magnitude uncertainties. Here we used the Kroupa mass function (Kroupa 2001), King profile (King 1962) and PARSEC models (Bressan et al. 2012) for DECam filters (g, r and i). The positions of the synthetic stars are randomly chosen from the King profile for some choice of r_c, r_t and density normalization k. Their magnitudes are also randomly picked given the chosen isochrone model (age, metallicity, distance and reddening) and mass function. We used the same extinction law as cited above for DES bands and a typical magnitude error curve for each filter.

We simulated star clusters at a fixed distance modulus of $(m - M)_0 = 18.5$ and no reddening. The simulated clusters were all cut at $g \leq 24$ and $\sigma_{g,\,r,\,i} \leq 0.1$. These photometric uncertainties were assigned to the synthetic stars following empirical curves as a function of *gri* magnitudes taken from Balbinot et al. (2015). For simplicity, we did not simulate unresolved binaries. We also used a fixed concentration parameter typical of LMC clusters for all the simulations, $\log_{10}(r_t/r_c) = 0.6$ (Werchan & Zaritsky 2011).

We produced sets of clusters with different richness levels, varying the number of stars but keeping tidal radius constant (for a same set of simulations). Each set had six clusters, resulting from the combination of two bins in metallicity (metal-poor, $Z = 0.0002$; and metal-rich, $Z = 0.010$) with three bins in age (young, 1 Gyr; intermediate age, 5 Gyr; and old, 10 Gyr).

All clusters in a set were simulated with a variable number of input stars in GENCMD. The final number depends on several factors, including distance, magnitude and colour cut-offs, photometric errors, age and metallicity. A first set was run for clusters with a total of 1200–5400 input stars following a King profile with $r_t =$ 94 arcsec. The number of stars in the output varied from 88 to 151. Fig. 4 presents the results for application of the method for a simulated cluster with τ = 5 Gyr, $Z = 0.010$, r_c = 20 arcsec, r_t = 94 arcsec and 137 stars, centred in the image centre. The recovered structural parameters are r_c = 20 arcsec and r_t = 96 arcsec and the best-fitting centre is offsets $\Delta x = 4.3$ arcsec and $\Delta y = 0.6$ arcsec, using the method described above (Section 3). The method is also very efficient in recovering the input isochrone (Fig. 5, upper panels).

To probe the limitations of the methods to cluster richness we simulated additional, poorer clusters. One of these runs simulated six small clusters (r_t = 48 arcsec), with 21–38 stars in the output, following the same ratio ρ_c/N (ρ_c = central density and N the cluster total star count). As shown in the bottom panel

---

[1] https:/github.com/balbinot/genCMD

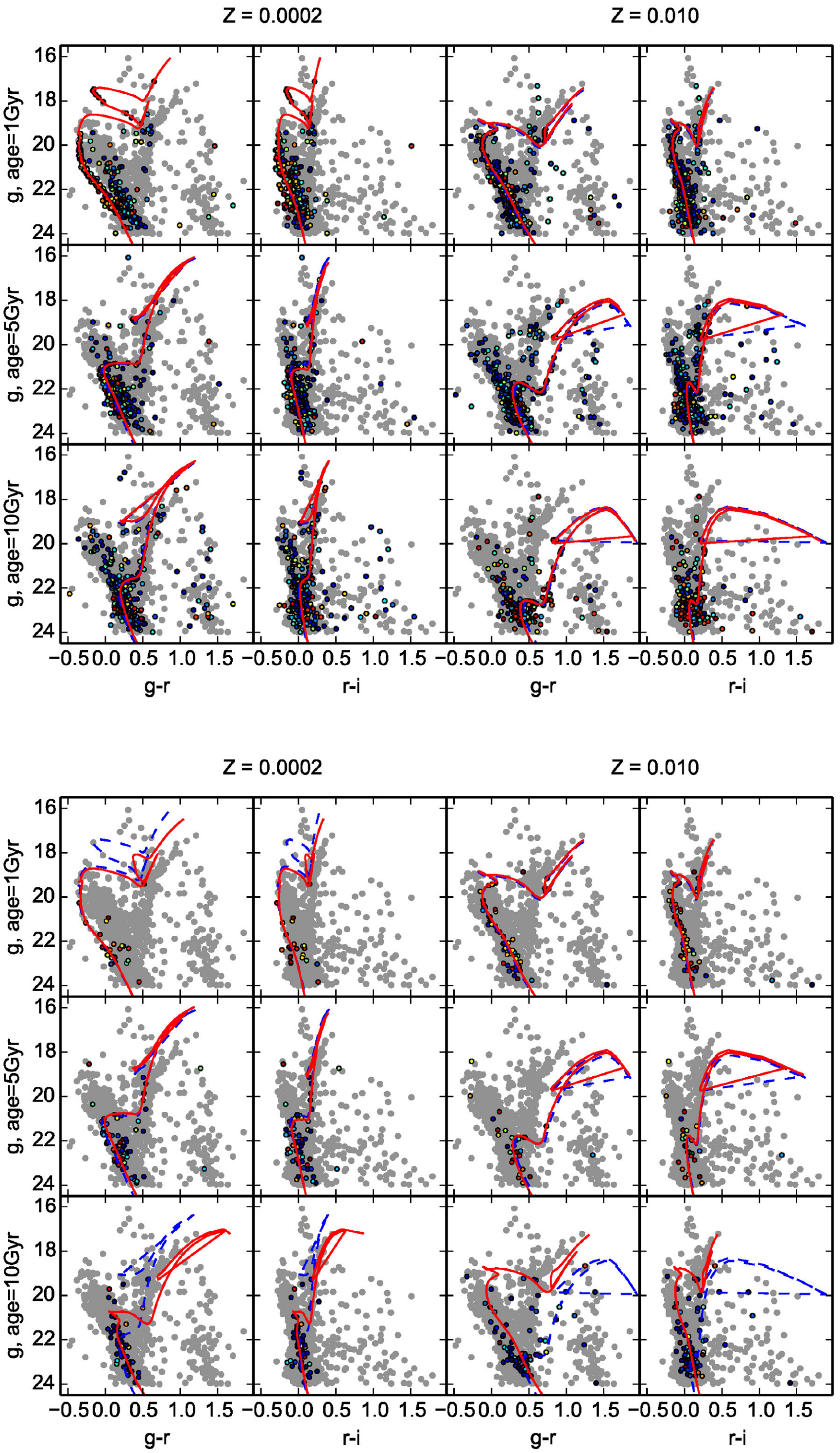

Figure 5. Synthetic CMDs for six clusters inserted in an LMC field in three bands (*g*, *r* and *i*). The clusters are combinations of young (1 Gyr), intermediate age (5 Gyr) and old ages (10 Gyr) with two metallicities ($Z = 0.0002$ and 0.010). Stars whose likelihood to belong to a cluster is greater than 0.05 are shown in colour (and black outline), while background stars are shown in grey. The generating isochrone (dashed blue line) and the recovered isochrone (solid red line) are overlaid to the data. Top: clusters with 88–151 stars. Bottom: clusters with 21–38 stars. The method fails to recover cluster parameters of old and sparse clusters (clusters with 22 and 36 stars, respectively). Young and intermediate age clusters (which represent the majority of LMC clusters sample) are well recovered even for a small number of stars.

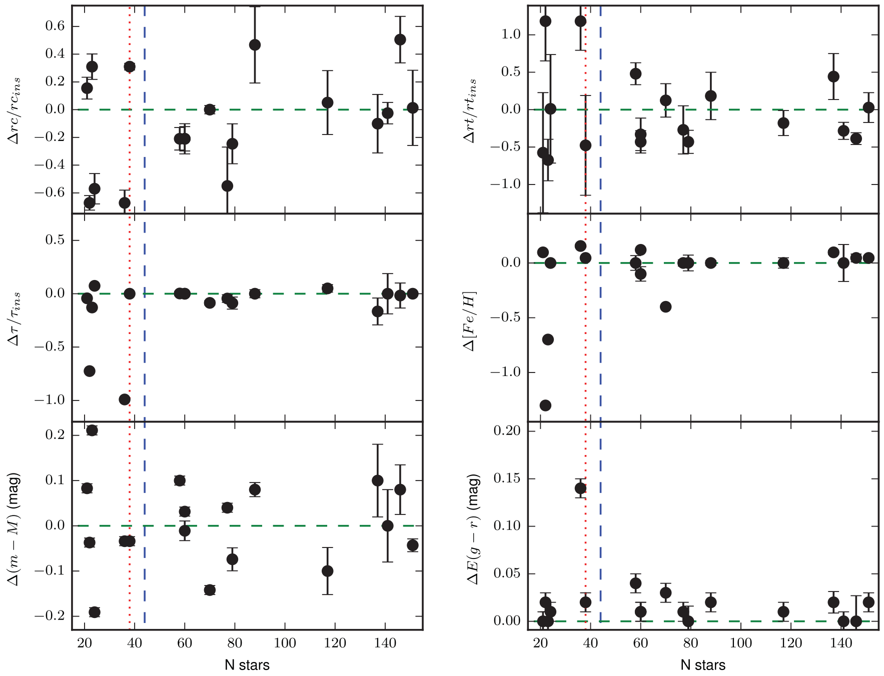

Figure 6. Errors in parameter recovery as a function of number of stars in simulated clusters. Top panels: relative errors in core radius and tidal radius; middle panels: relative errors in age and absolute error in metallicity; bottom panels: errors in distance modulus and $E(g-r)$, in magnitude units. The dashed blue line shows the adopted minimum cluster richness of 44 stars in the actual LMC sample.

of Fig. 5, the method fails to correctly recover the old clusters (which have, respectively, 22 and 36 stars for the low and high metallicities).

The errors in recovering cluster parameters for all our simulated sets are addressed in Fig. 6; we show the relative parameter errors, as well as the estimated uncertainties. For the vast majority of simulated clusters, the figure shows errors of <20 per cent in age and metallicity, <10 per cent in distance, and <0.05 in extinction. The structural parameters are recovered with somewhat larger errors, ≃40 per cent. There is a weak dependence of the error amplitude on cluster richness in most panels. This trend is more visible in the r_t, age and [Fe/H] plots, where errors significantly larger than those quoted above occur for simulated clusters poorer than $N \simeq 40$–50. A similar behaviour is also seen in the CMD fits presented in Fig. 5, as discussed earlier. To prevent lower quality fits from contaminating our results, we adopt a somewhat arbitrary lower limit in richness of $N = 44$ in our LMC sample. We note, however, that we have only 20 clusters (≃17 per cent of the sample) in the range 44–100 stars, and that no visible trend in age, [Fe/H], distance modulus, redenning or structural parameters is seen in this richness range. This renders the results of our upcoming analysis (Section 5.2) robust to the exact richness threshold adopted.

5 DES-SV DATA

In this section, we show the results of our profile and isochrone fitting methods to the sample of LMC clusters. We first carried out the profile fit as described in Section 3.1. Only clusters with a $\mathcal{L}$ peak corresponding to r_t < 6.5 arcsec and with a minimum of $N_{star} = 44$ member stars were used in the subsequent analyses. The upper bound in the tidal radius is the size of the co-add image cutout around each cluster candidate. The only exception to this rule is the Reticulum cluster, whose tidal radius is larger than the image cutout size but was kept in our sample for comparison with results from the literature (Section 5.1). The richness criterion is guided by our simulation results, as discussed in Section 4. Of the 255 cluster candidates mentioned in Section 2.2, only 121 had their structural parameters successfully determined by the likelihood fit. Including the Reticulum cluster (122 candidates), the final sample available for isochrone fitting and analysis amounts to 117 clusters. Five clusters have less than the adopted minimum number of member stars and are therefore below the threshold limit.

Fig. 7 presents their on-sky distribution colour coded by their most likely tidal radius.

5.1 Comparison to literature

Before proceeding with an LMC cluster system analysis, we first validated the methods outlined in Section 3 with DES-SV data by comparing our LMC clusters parameters to those found in the literature. Our comparison sample is made up of six relatively rich clusters for which data of comparable or superior quality are available. For NGC 1868 and NGC 2162, there are parameter estimates from more than one source in the literature, while for Hodge 4, ESO 121-03, NGC 2193 and Reticulum cluster only one reference was found. The results are summarized in Table 1 and Fig. 8.

The results listed in Table 1 come from a variety of different methods and data. Most of them are based on CMD analysis, like our own. In this sense, the fits found in previous works are not necessarily more accurate than ours. In particular, none of those papers are based on the same set of PARSEC isochrones used in this work and some of them are not based on optical data, as is the case of Grocholski et al. (2007). These issues, coupled with variations in methodology, are probably the cause of the spread in the parameters from different authors, or even among the same authors, as attested by the compilation of NGC 1868 and NGC 2162 results. Even with this spread, there is a clear correlation

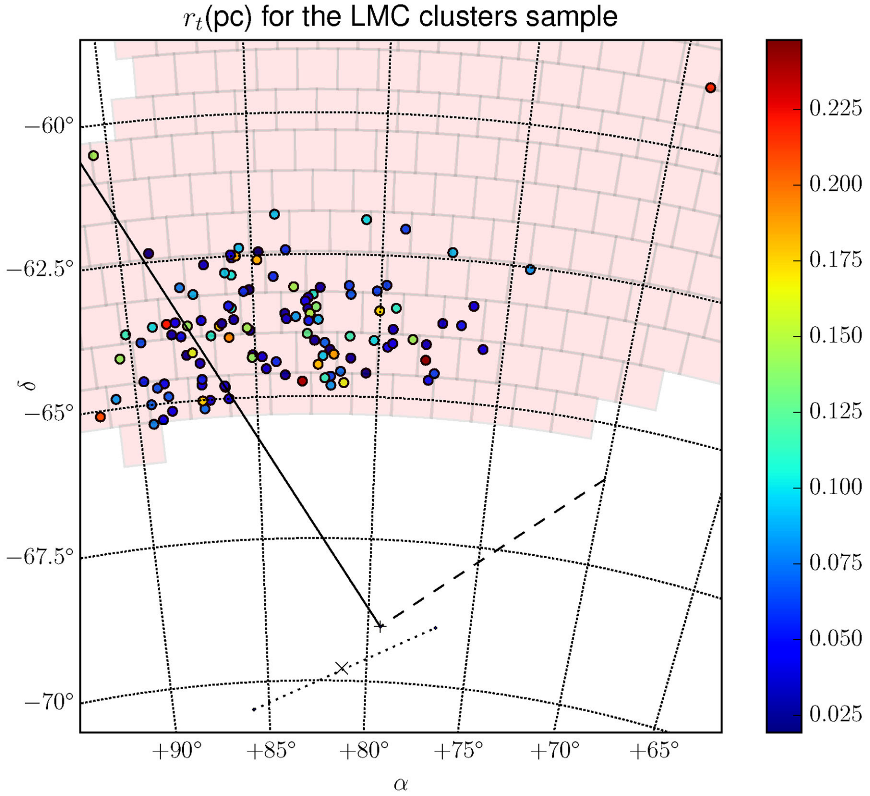

Figure 7. On-sky cluster sample (circles), showing the distribution of tidal radius (in parsecs, colour coded) and the tiles sampled (complete or incompletely) in SV campaign (red boxes). The cross (bottom) indicates the LMC centre as assumed here. The dashed line is the LMC line of nodes and solid line is the maximum gradient distance line. From van der Marel (2001), we present the location of LMC bar (dotted line as the major axis) and its centre ('x') in the maximum star surface density. The Reticulum cluster is the upper rightmost cluster.

between our fits and literature, as one can see in Fig. 8 for all the parameters. Fig. 8 testifies that there is no strong systematic trends in our determinations. Therefore, we conclude that the soundness of our methodology is further corroborated based on these real data comparisons.

For the structural parameters, we had no overlap with the large sample of clusters measured by Werchan & Zaritsky (2011). The only paper with a common sample is Mackey & Gilmore (2003), who measure surface brightness profiles compared to our star density profiles. The authors describe how it is difficult to reconcile their results with density profiles in the literature. A possible explanation for this discrepancy is incompleteness, which affects the density profile much more than surface brightness profiles, since fainter stars have low weight in surface brightness profile while in density profiles all stars have the same weight. The incompleteness severely affects crowded systems, as NGC 1868 and NGC 2162, for which we find core radii 15 and 5 times larger, respectively, than Mackey & Gilmore (2003). For Hodge 4 (a less crowded cluster), this ratio decreases to 3 times larger.

In Fig. 9, we show completeness curves in *gri* bands integrated over the entire cutout of SL 262. We also show completeness curves in the centres of moderately and severely crowded clusters, namely SL 262 and NGC 1868. For that purpose, we picked a square image (54 × 54 arcsec) centred in each cluster. For clarity, curves are only presented for *g* band, but are similar at other bands. The completeness levels shown correlate well with the strong discrepancies we find with respect to Mackey & Gilmore (2003) and suggests further that incompleteness is the dominant source of these discrepancies. Note that rich clusters which have crowded centres make up about 15 per cent of our sample.

The completeness was estimated in our data by inserting 2.4×10^4 artificial stars in 10 realizations of the image in each band (*g*, *r* and *i*) for the two clusters cited above. We then proceeded to reduce the artificial stars in the same manner as the DES-SV data. The inserted stars vary in the range $21.0 \leq g \leq 25.0$. The criteria to recover stars are the same used to classify a source as star: $\mathrm{error}_{g,\,r,\,i} \leq 0.1$ and $|\mathrm{sharpness}_{g,\,r,\,i}| \leq 1.0$, and a maximum deviation from initial position equal to 0.8 arcsec.

To test whether the differences between our estimate of the core radius and those in the literature might stem from completeness, we used the same maximum likelihood method for the NGC 1868 profile, but selecting only stars with $g < 21.5$. The corresponding core radius using the latter sample (less affected by incompleteness) decreased to 0.58 of the value initially measured (using stars with $g < 24$). The tidal radius increased 10 per cent (certainly due to statistical variations, given the lower star counts in cluster outer regions). We then conclude the completeness is the main cause of difference between our determinations and those from Mackey & Gilmore (2003).

5.2 DES-SV LMC clusters

In this section, we analyse the distribution of LMC clusters as a function of size, age, metallicity and position in space.

Figs 10 and 11 show the results of the ML method for SL126, which is a typical cluster from our sample. Fig. 10 has a clear

Table 1. Table comparing literature data and our determinations. Numbers in superscript indicate the references, while the last line to each cluster shows the values determined in this paper.

Cluster	log(age)	[Fe/H]	$E(g-r)$	$(m-M)_0$	r_c(arcsec)
NGC 1868	8.87 ± 0.10^a				6.67^b
	8.74 ± 0.30^c	-0.50 ± 0.20^d			
	8.95 ± 0.03^e	-0.40 ± 0.10^e			
	8.97 ± 0.04^f	-0.32 ± 0.71^f			
	8.95^g	-0.38^g	0.00^g	18.70^g	
	8.93^h	-0.38^h	0.04^h	18.45^h	
	9.05 ± 0.03^i	-0.70 ± 0.10^i	0.04 ± 0.01^i	18.33 ± 0.06^i	
	9.10 ± 0.01	-0.88 ± 0.04	0.09 ± 0.02	18.35 ± 0.01	99
NGC 2162	8.95 ± 0.10^a				10.13^b
	9.20 ± 0.12^j	-0.40^k			
	9.32 ± 0.06^f	-0.90 ± 0.03^f			
	$9.11^{+0.12\,l}_{-0.16}$	-0.23 ± 0.20^k			
	9.10 ± 0.03^i	-0.38^i	0.03 ± 0.02^i	18.35 ± 0.08^i	
	9.15^m	-0.46 ± 0.07^m	0.03^m	18.58 ± 0.18^m	
	9.11 ± 0.01	-0.88 ± 0.06	0.08 ± 0.02	18.36 ± 0.01	55
Hodge 4	9.33^m	-0.55 ± 0.06^m	0.04^m	18.37 ± 0.03^m	15.2^b
	9.37 ± 0.02	-0.88 ± 0.06	0.01 ± 0.02	18.53 ± 0.02	50
ESO121-03	9.95^m	-0.91 ± 0.16^m	0.03^m	18.12 ± 0.06^m	
	9.99 ± 0.01	-1.40 ± 0.05	0.07 ± 0.01	18.35 ± 0.01	
NGC 2193	9.30^m	-0.49 ± 0.05^m	0.04^m	18.45 ± 0.04^m	
	9.38 ± 0.01	-0.70 ± 0.04	0.03 ± 0.01	18.35 ± 0.01	
Reticulum cluster		-1.70 ± 0.10^h	0.00^h	18.37 ± 0.07^h	
	$10.11 - 10.18^n$	-1.44^n	0.016^n	18.40^n	
	10.10 ± 0.01	-1.88 ± 0.10	0.00 ± 0.01	18.49 ± 0.01	

[a] Girardi et al. (1995) (CMD fitting),
[b] Mackey & Gilmore (2003) (Surface brightness profiles),
[c] Elson & Fall (1988) (CMD fitting),
[d] Olszewski et al. (1991) (spectroscopy of red giants),
[e] Kerber & Santiago (2005) (HST/CMD fitting),
[f] Leonardi & Rose (2003) (integrated spectra),
[g] Kerber & Santiago (2006) (HST/CMD fitting),
[h] Li, de Grijs & Deng (2014) (CMD fitting and simulations),
[i] Kerber et al. (2007) (HST/CMD fitting),
[j] Piatti et al. (2014) (HST/CMD fitting),
[k] Piatti et al. (2013) (CMD fitting),
[l] Geisler et al. (1997) (CMD fitting),
[m] Grocholski et al. (2007) (RC and CMD fitting),
[n] Kuehn et al. (2013) (Variable stars).

$\log(\mathcal{L})$ maximum for the profile and indicates that we successfully recovered the centre and the structural parameters of this cluster. The CMDs in Fig. 11 are well described by the best-fitting isochrone that resulted from the method described in Section 3.2.

The concentration and $\log_{10}(\frac{\rho_c}{\rho_{\rm bg}})$ histograms are shown in Fig. 12 for all clusters. The concentration distribution is very similar to the one shown by Werchan & Zaritsky (2011, top panel of their fig. 14), which is based on fits to radial luminosity profiles. Both display a broad peak around $c = 0.6$, and another peak at very low concentration values. In our analysis this latter peak is not as pronounced, probably attesting a strong selection bias in favour of clusters with high contrast to background (in this work), which will tend to be more concentrated at a fixed richness. Another reason for this mild discrepancy is that the authors used a radius encompassing 90 per cent of luminosity rather than the tidal radius.

The central density relative background histogram has a peak $\simeq$3.5 times background density. A small number of clusters have densities near the background value; these are mainly located closer to the LMC centre. In contrast, the high values for central densities usually occur for clusters located farther from the LMC centre. The most notable cluster in this sense is the Reticulum cluster, which is located in a region where the stellar density is very low. This cluster does not have a crowded central region, allowing for good photometric parameter estimation.

The age distribution of the LMC clusters in our sample presents two main peaks, at ∼1.2 and ∼2.7 Gyr. This can be seen in Fig. 13 (top-right panel). The same figure also shows ages as a function of position on the sky (top-left panel) and distance to the LMC centre (r; bottom-left panel). No obvious age gradient is seen in this latter plot.

To assess the significance of the observed bimodality, we carried out Kolmogorov–Smirnov (KS) tests based on the null hypotheses that the observed distribution is either single or doubled peaked. We limited the test to clusters with <4 Gyr (114 clusters from the total of 117 clusters). We fitted the observed age distribution to models with one and two Gaussians. We then created 1000 random

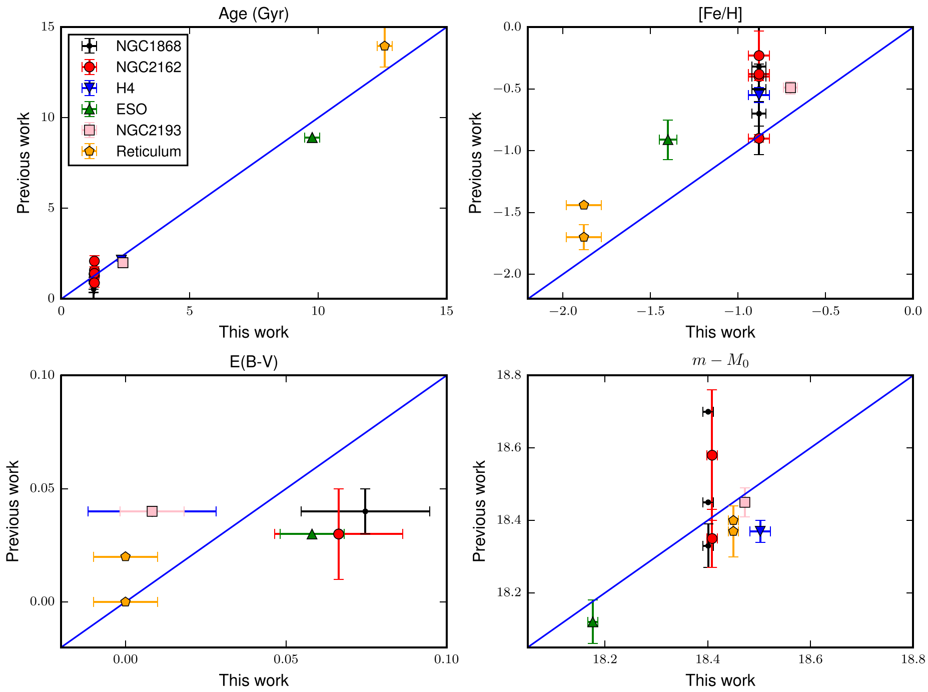

Figure 8. Comparison between our fits and previous works for age (upper left), metallicity (upper right), reddening (lower left) and distance modulus (lower right). The identify line is also plotted. The uncertainties are shown in the cases they were quoted in the references.

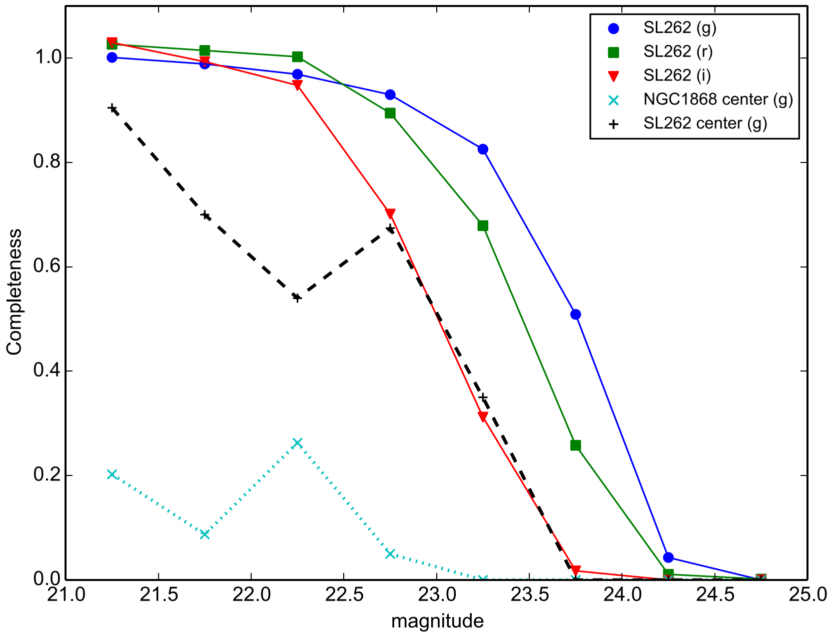

Figure 9. Completeness curves integrated over all positions in the SL 262 cutout ($\simeq$6.6 arcmin) are shown for g, r and i bands (solid lines: circles, squares and triangles, respectively). Completeness covering central regions (a square with 53 × 53 arcsec) of SL262 (moderate crowding, dashed line and plus symbols) and NGC 1868 (severe crowding, dotted line and cross symbols) is shown just for g band as dotted lines, plus and star symbols, respectively.

samples of ages with the same size as the real sample and following each of these models, and applied the KS test comparing each realization to the real distribution. The average result over 1000 realizations indicates that the real clusters do not originate from a unimodal distribution ($\bar{p} = 0.009$ or $\simeq 3\sigma$). Therefore, we can reject the hypothesis that the real age distribution comes from a unimodal distribution.

For the double Gaussian model, the best-fitting age peaks confirm the visual estimates, corresponding to 1.2 and 2.7 Gyr, respectively. And the average p-value over 1000 realizations is 0.25, showing that the observed distribution is consistent with the adopted null hypothesis in this case.

The Gaussian mixture model fit indicates two Gaussian for the age distribution (114 clusters with age <4 Gyr) using Bayesian

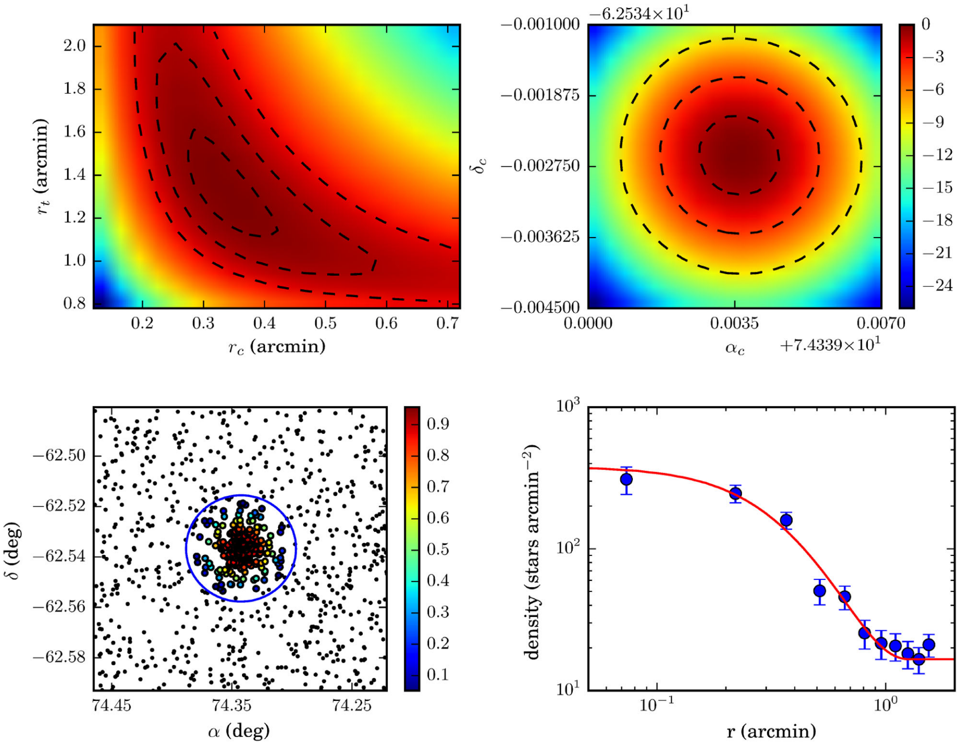

Figure 10. Maximum likelihood method applied to the cluster SL126. The most likely parameters for this cluster are $r_c = 19$ arcsec, $r_t = 79$ arcsec, $\alpha_c = 74\overset{\circ}{.}3424$, $\delta = -62\overset{\circ}{.}5356$, $k = 0.14$ stars arcsec^{-2}. Top panels: likelihood distribution (normalized by maximum) over r_c and r_t (left) and over cluster centre coordinates (right). Lower left: field stars ($P^{\mathrm{kp}} < 0.05$, black dots) and likelihood (colour bar) that each star belongs to the cluster. Lower right: density profile binned in 11 rings (blue dots) and the fitted density profile (solid red line).

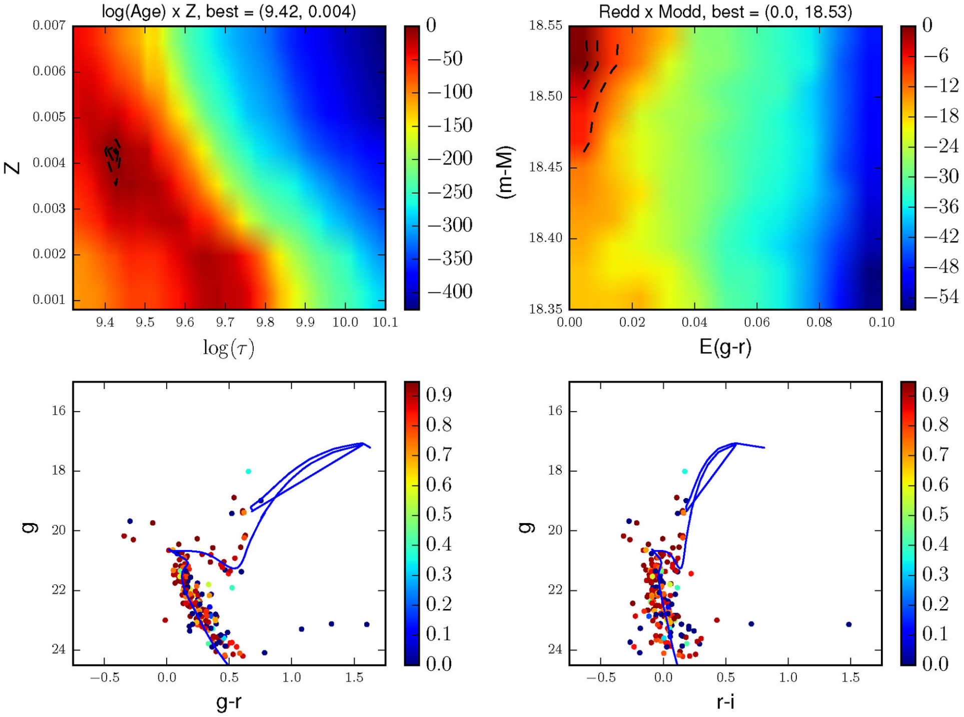

Figure 11. 2 log($\mathcal{L}$) distribution for age and metallicity (top-left panel) and for reddening and distance modulus (top-right panel) for cluster SL 126 (scaled as coded in the colour bars). The bottom panels show g versus $(g - r)$ and g versus $(r - i)$ CMDs. Only stars with membership probability, $P^{\mathrm{kp}} > 0.05$, are shown. The best-fitting isochrone (given by MLE) is also overlaid.

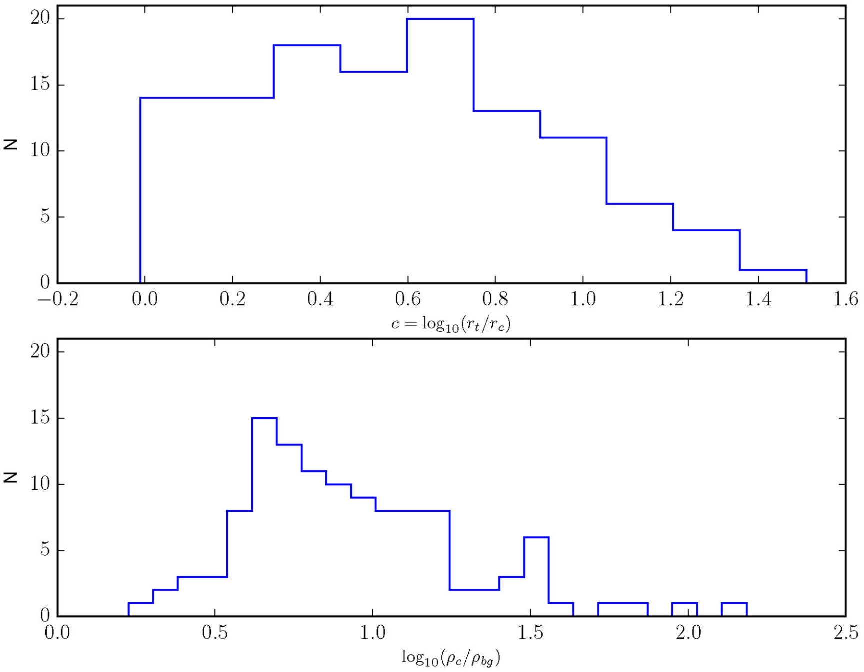

Figure 12. Distribution of concentration parameter (top) and of the logarithm of central density contrast over the background (bottom) for the LMC clusters sample.

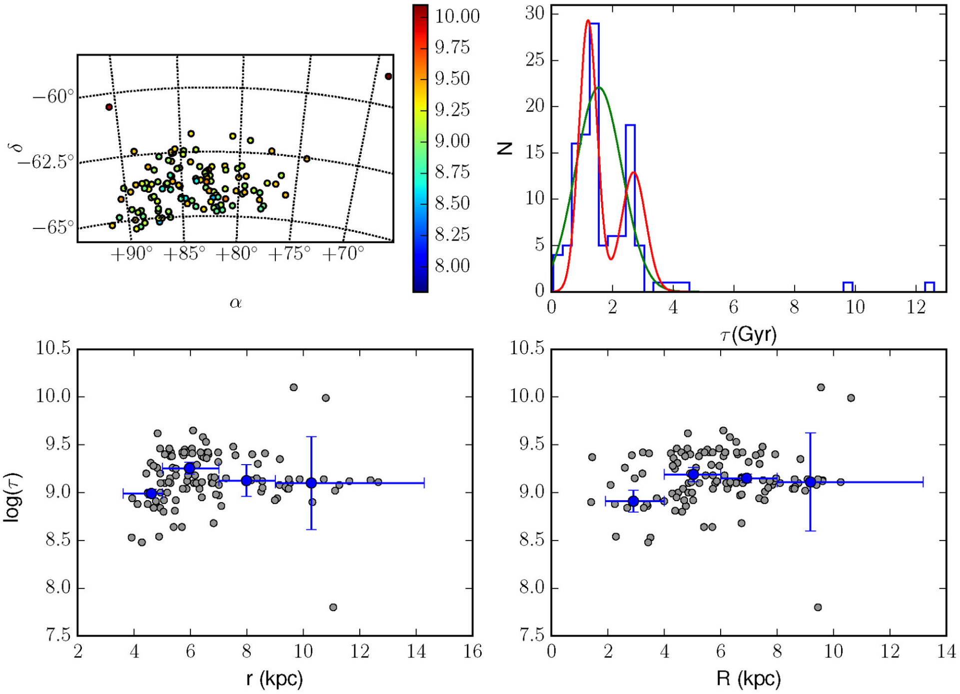

Figure 13. Top left: on-sky cluster distribution colour coded according to log(age). Top right: histogram of cluster ages shown along with unimodal and bimodal Gaussians fitted using the method presented in Ashman, Bird & Zepf (1994). Bottom left: age versus radial distance from LMC centre. Blue circles present the median age in four non-equal subsamples. Horizontal bars indicate the coordinate range. Vertical bars represent the standard deviation in age for each subsample. Bottom right: age versus cylindrical coordinate *R*.

information criteria (BIC). We found relative weights of 0.63 and 0.37 for these Gaussians centred in 1.1 and 2.3 Gyr with standard deviations of 0.4 and 0.6 Gyr, respectively. BIC returns as best values 258.8 for two Gaussians against 268.2 for three and 270.4 for only one Gaussian.

We also tried to follow the recipe in Ashman et al. (1994) to investigate the best-fitting multipeak model for the observed age distribution in the sample. However, our fits for one, two and three Gaussians resulted in different standard deviations: 0.43 and 0.3 Gyr for two peaks, and 0.44, 0.12 and 0.16 Gyr for three peaks. The lack

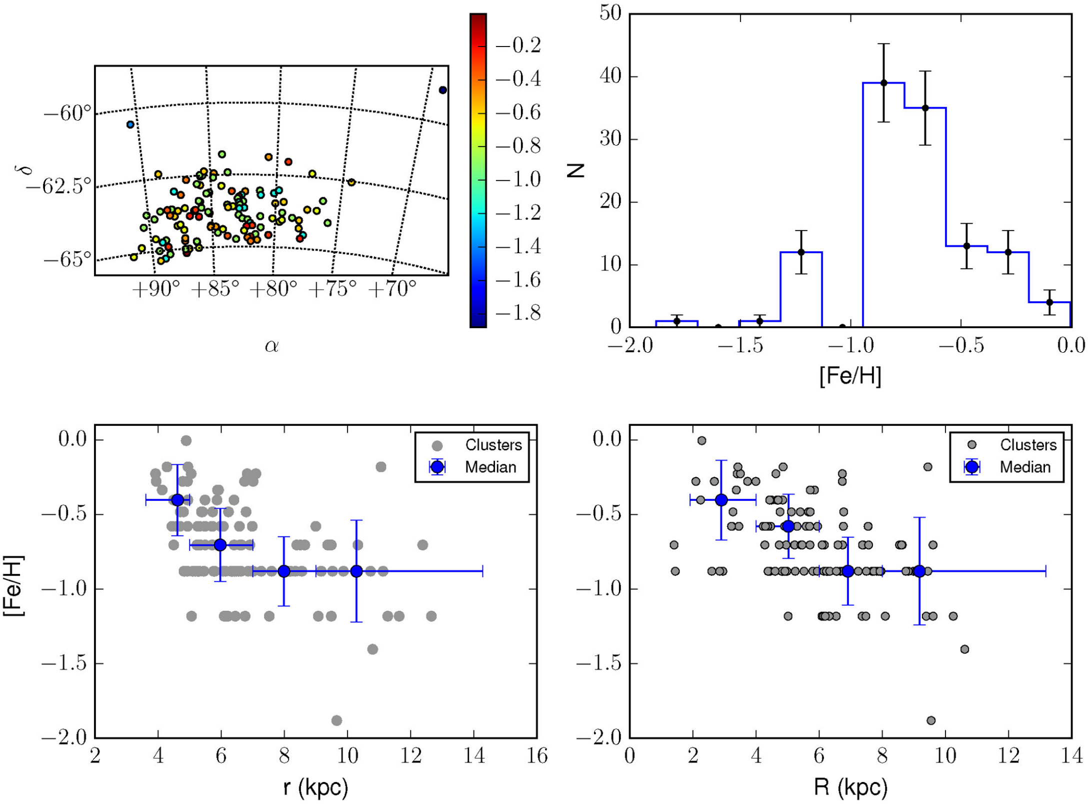

Figure 14. Top left: on-sky cluster metallicity distribution (colour coded). Top right: metallicity histogram. Bottom left: [Fe/H] versus radial distance from LMC centre (grey circles). Filled circles present the median for metallicity, dividing the distance range in four non-equal subsamples (blue dots are placed at each subsample median distance). Vertical bars represent the metallicity dispersion (standard deviation) for each subsample. Horizontal bars are the subsample range in radial coordinate (r or R). Bottom right: metallicity (Fe/H) for cylindrical coordinate R (radial distance projected on disc).

of homoscedastic distributions in the current situation rendered any the results from the method by Ashman et al. (1994) less reliable, as discussed in Ashman et al. (1994) and Nemec & Nemec (1991).

Given the observed bimodality in the age distribution, we split the sample into two classes, of clusters younger and older than 2 Gyr. We calculated a mean r for these two age classes, obtaining $\bar{r} = 6.87$ and 6.42 kpc, respectively.

We also computed cylindrical coordinates of each cluster based on an LMC disc model from Balbinot et al. (2015). These authors fit the DES-SV field stars distribution and derive the disc position angle and inclination with respect to the sky. The LMC centre and heliocentric distances were kept fixed in the fit at $\alpha_0 = 79\overset{\circ}{.}40$, $\delta_0 = -69\overset{\circ}{.}03$ (Nikolaev et al. 2004) and $D_{\rm LMC} = 49.9$ kpc (de Grijs, Wicker & Bono 2014). To determine the cylindrical coordinates, we used the transformations presented in Weinberg & Nikolaev (2001). In the lower-right panel of Fig. 13, we plot the ages against the R coordinate, along the disc plane, and again infer an essentially flat relation. The $\overline{R}$ values for our two age subsamples are 5.92 and 5.79 kpc for the younger and older clusters, respectively.

Our sample covers an unprecedented range in distances from the LMC (from ≃4 kpc out to ≃13 kpc), reaching out to previously unexplored outer LMC regions. The clusters age distribution presented here is complementary to that shown by Piatti & Geisler (2013), who study field stars in regions corresponding to deprojected distances in the range from ≃0.5 kpc out to ≃8 kpc. Those authors favour an outside-in star formation in the sense that old (and metal-poor) stars tend to be located in the outer disc, whereas younger stars (also more metal-rich) tend to inhabit the inner LMC regions. This age trend with distance, however, is largely restricted to the inner 4 kpc. Beyond that, their relation between age and distance is flat, similar to what is found with the LMC clusters studied here.

Fig. 14 shows similar plots for metallicity. Most clusters in our sample are metal poor $Z < 0.004$ ([Fe/H] < -0.7) as Fig. 14 shows in upper-right panel. Unlike age, there is a clear trend in metallicity as a function of distance from the LMC centre (bottom panels). The two-sided p-value for a statistical hypothesis test (whose null hypothesis is that the slope is zero) is 10^{-8} for R and 10^{-6} for r. We conclude we can reject the null hypothesis.

The median metallicity systematically drops by a factor of ≃2 from $r = 5$ to 10 kpc. Clusters with $-1.5 <$(Fe/H)< -1.0 are distributed over the entire radial distance range. On the other hand, $Z > 0.005$ clusters ([Fe/H] > -0.6) are only found for $r < 8$ kpc. A larger metallicity spread in inner fields has also been found by Piatti & Geisler (2013) for LMC field star population. However, for the range of distances in common with their study, our results are in disagreement in the sense that the clusters have a larger spread than the field stars at a fixed distance from the LMC centre.

The AMR is plotted in Fig. 15, where we compare the AMR from our data (blue filled dots) to the one from Piatti & Geisler (2013, open boxes for LMC field stars and filled boxes for LMC clusters). In general, the AMR from those authors corresponds to an upper envelope to the cluster AMR presented here. In particular, our sample includes young clusters with a very large range in metallicities, reaching down to [Fe/H] ≃−1.2. These are mainly the clusters belonging to the 1.2 Gyr age peak. This young and metal-poor sample is consistent with a recent cluster formation epoch in the outer

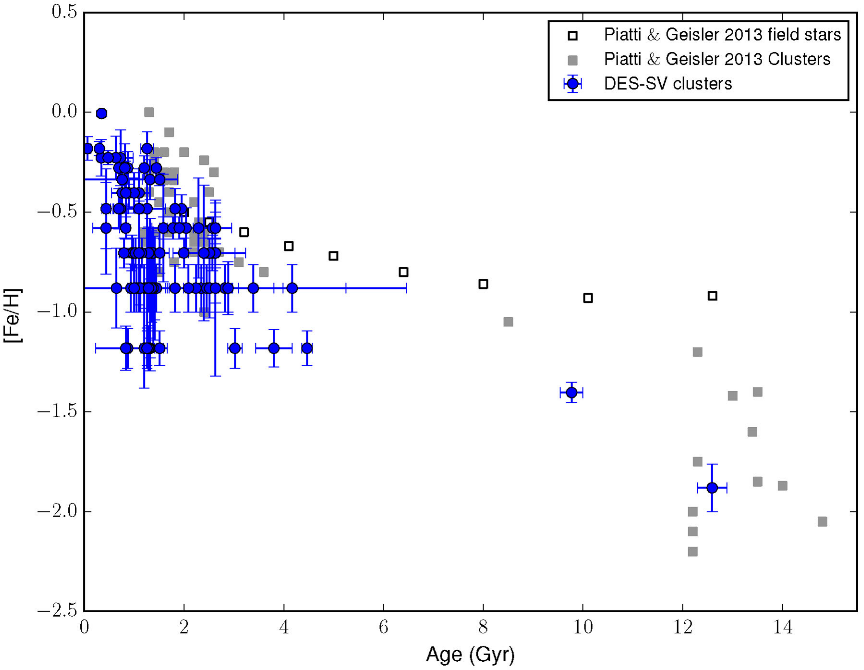

Figure 15. AMR for LMC clusters sample (filled circles). Open boxes (field) and filled boxes (clusters) are from Piatti & Geisler (2013, fig. 6 in that paper).

regions of the LMC sampled in this paper, contrasting a relative low SFR in these areas (Meschin et al. 2014). This large spread at relatively young ages contrasts with the lack of metal-rich clusters at larger ages.

Our results are in agreement with Livanou et al. (2013), who analysed a sample of 15 LMC clusters spread all over the galaxy. On the other hand, the field stars AMR relation from Carrera et al. (2011) lead to higher metallicities at a fixed age than those typically inferred for our sample of outer LMC clusters, at least for ages >3 Gyr. The discrepancy is not caused by the different ranges in distance to the LMC centre, since most of our clusters are closer to 8 kpc, similarly to their sample. This is another example of a discrepancy between results based on field and cluster stars.

In Fig. 16, we compare the AMR for our sample of outer LMC star clusters to the most accepted models used in literature for the LMC chemical evolution. Briefly, the model from Pagel & Tautvaisiene (1998) is based on a bursting model assuming a constant star formation rate for clusters in the range $1.6 < \tau < 3.2$ Gyr. In that model, the metallicity increases for clusters younger than 1.6 Gyr and this feature reasonably describes the upper metallicity limit for the younger clusters studied here, as well as the old and most metal-poor clusters. The Harris & Zaritsky (2009) model is based on the STARFISH analysis code, using bright field stars. Their results describe an initial burst of star formation and a quiescent epoch from approximately 12 to 5 Gyr ago. Star formation then resumed and has proceeded until the current time at an average rate of roughly 0.2 $\mathrm{M_\odot\,yr^{-1}}$. Among the global variations in the recent star formation rate they identify peaks at roughly 2 Gyr, 500, 100 and 12 Myr. This latter model better represents the younger clusters in our sample. Palma et al. (2015) study a sample of clusters located in an inner LMC region and whose AMR is bracketed by the two models. Those authors argue that a combination of both models is a more adequate description of their sample than a single model. Our sample, on the other hand, shows a sizable fraction of relatively young clusters with lower metallicities than predicted by either model.

Fig. 17 shows the results for the reddening values obtained from the ML fits. The sample of clusters is systematically decreasing towards larger extinction. The majority of the clusters have $E(g-r) \leq 0.10$. Using the maps from Schlegel, Finkbeiner & Davis (1998) and the reddening law from Cardelli et al. (1989), the typical values towards these clusters are in the range $0.04 \leq E(g-r) \leq 0.10$, which is in general agreement with the fitted values. There is no strong trend in $E(g-r)$ values with distance from the LMC centre.

6 DISCUSSION AND SUMMARY

Here we summarize our main results.

(i) We scanned the DES-SV images to search for stellar overdensities in fields close to the LMC, identifying 255 cluster candidates. We catalogued and matched this sample to the star clusters catalogue from Bica et al. (2008), adding clusters already discovered and identifying unknown clusters. We used DES-SV co-add images in g, r and i bands to make square cutouts (with 6.75 arcmin on a side) around each candidate.

(ii) We found that stellar completeness in DES-SVA1 catalogue is a strong function of source density, sharply dropping to <0.1 for surface densities >260 stars $\mathrm{arcmin^{-2}}$. The DES-SVA1 stellar sample is very incomplete in crowded fields, such as those close to centres of rich LMC star clusters, where DESDM detects less than 50 per cent of the objects detected by DAOPHOT.

(iii) To reduce stellar incompleteness in crowded fields, we developed a pipeline to reduce data using DAOPHOT. The pipeline combines g and r images and runs PSF selection and photometry in a largely automatic way. Using stars with good photometry in both catalogues, we compared the final DAOPHOT magnitudes to DES-SVA1, determining a zero-point. The agreement is very good and on average DES-SVA1 and DAOPHOT photometry agree within

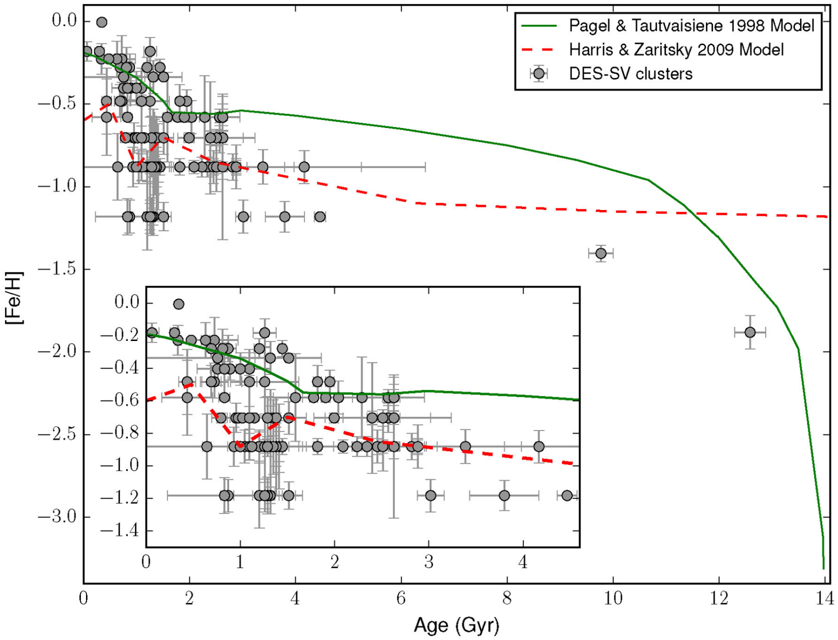

Figure 16. Two models for the LMC chemical evolution history are compared to the AMR for outer LMC clusters (filled circles). The model from Harris & Zaritsky (2009) is shown as a dashed red line, whereas the solid green line shows the Pagel & Tautvaisiene (1998) model. Box: zoom in over the region indicated, showing the young and metal-rich clusters compared to both models.

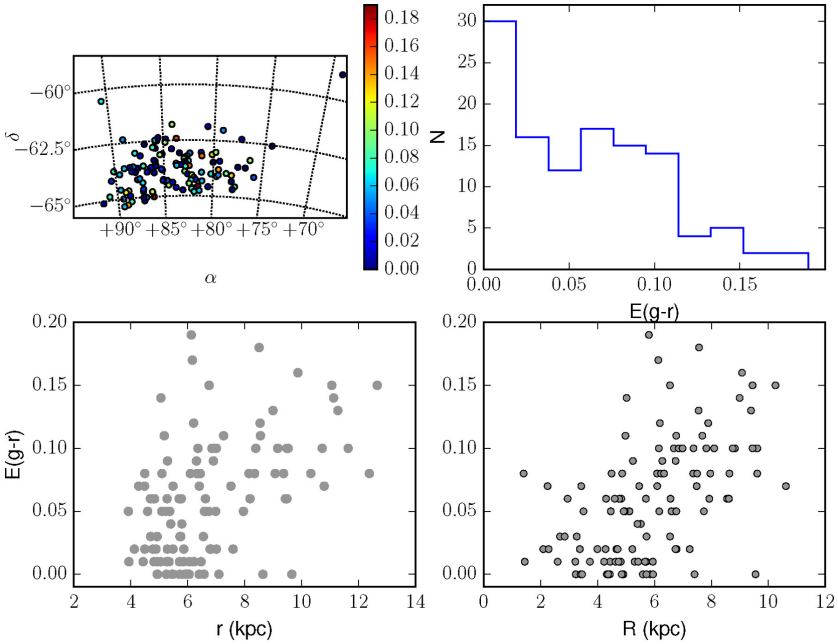

Figure 17. Top left: on-sky cluster distribution colour coded according to $E(g-r)$. Top right: distribution of $E(g-r)$. Bottom: reddening versus radial distance from LMC centre (left) and versus cylindrical coordinate R (radial distance projected on disc) at right.

0.02 in three bands, without the need for a colour term. We selected stars as sources from DAOPHOT reductions with g,r,i errors <0.1 and $|\mathrm{sharpness}_{g,r,i}| < 1$.

(iv) We applied a maximum likelihood estimation approach to fit the stellar density profile to a King model (King 1962), following a recipe similar to that of Martin et al. (2008). This method is robust to determine centre position, core and tidal radii. As output, for each cluster candidate we listed the stars within the tidal radius, along with their probability to belong to cluster candidate (P^{kp}). From the initial sample containing 255 cluster candidates, only 121 had their structural parameters successfully determined by the profile likelihood fit.

(v) We compared the stars with $P^{\mathrm{kp}} > 0.05$ to Bressan et al. (2012) isochrones, varying reddening and distance moduli in a two-step refined grid search. The final grid allows a more refined scan of parameters space around the MLE peak given by the initial grid.

The uncertainties are estimated from the likelihood distribution around peak. We used the results from this method for both global and structural parameters.

(vi) We tested our inference methods, by inserting simulated cluster stars (using GENCMD) in a typical LMC field and proceeding through the same steps as for real clusters. We varied the input number of simulated stars, reaching a minimal number of $\simeq$40–50 cluster stars necessary to recover the generating isochrone. When a threshold on the minimum number of stars is applied, the LMC cluster sample decreases from 121 to 117 clusters, which is the final number of clusters used in the analysis.

(vii) We compared our method to results from data from the literature. The agreement is usually within the uncertainties, with a few exceptions in distance modulus, metallicity and core radii, and an excellent agreement for ages and reddenings. None of the comparison papers from the literature are based on the same set of PARSEC isochrones used in this work or even in optical data. These issues and the variations in methodology, are probably the cause of the discrepancy in the parameters from different authors. Given we are dealing with a homogeneous photometric sample, we conclude that our method is corroborated based on these real data comparisons (literature and our results).

(viii) The cluster age distribution presents two main peaks in 1.2 and 2.7 Gyr. We run statistical KS tests to probe the bimodality significance. The tests confirm that a two-peaked age distribution is more consistent with the observed distribution, and rule out that the data follow a single peak age distribution. Splitting the sample in clusters younger and older than 2 Gyr and calculating a mean radial distance to each subsample, the difference is not sensitive whether considering $\bar{R}$ (5.92 and 5.79 kpc) or $\bar{r}$ (6.87 and 6.46 kpc). This conclusion agrees to Piatti & Geisler (2013), who found a flat age-distribution for fields with radial distances >4 kpc.

(ix) Metallicity presents a clearer radial trend, both in terms of the average metallicity or its dispersion. Metal-rich clusters ([Fe/H] >-0.6) are concentrated within $r<8$ kpc, whereas the most metal-poor clusters are found over the entire distance range.

(x) The AMR for LMC clusters differs from LMC field stars AMR (from Piatti & Geisler 2013) in the sense that the latter form an upper envelope in metallicity for age distribution. The same feature is shown in Livanou et al. (2013), as the presence of young clusters (1 Gyr) filling the range from most metal rich down to [Fe/H] $\simeq-1.2$.

(xi) Regarding the LMC chemical evolution model, our sample shows more young metal-poor clusters than are predicted by the models of Pagel & Tautvaisiene (1998) and Harris & Zaritsky (2009). Apart from this, our results are in broader agreement with the models.

The discovery of 28 previously uncatalogued clusters (with profiles and models determined here) is proof that the list of LMC clusters is not complete, mainly in its less scrutinized outskirts.

It is expected that the final DES release will provide deeper photometry, reaching further into the clusters' MS and decreasing uncertainties for their SubGiant Branch and RGB stars, even the final release footprint will not cover same SV footprint. We plan to explore these data in greater depth, extracting more information about the LMC clusters, including the identification of extended main-sequence turnoffs, modelling binarism, better constraining their shapes and assessing the correlations among different cluster properties.

The cluster (and star) formation rate may be enhanced by tidal gravitational interactions (in this case, SMC-LMC or Galaxy-LMC). While the gravitational interaction between the Galaxy and the LMC is a controversial issue (see for example Kroupa & Bastian 1997; Kallivayalil et al. 2013), there is a consensus for the SMC-LMC orbit period being $\simeq$2 Gyr. In this sense, the age distribution of clusters as shown in Fig. 13 favours a strong gravitational interaction that occurred 1.5 Gyr ago, coinciding with the SMC-LMC pericentric passage predicted by the 'best orbital model' described in Bekki & Chiba (2005). The secondary peak at 3 Gyr is less pronounced, likely as a result of clusters disruption effects. Therefore, the relative peak heights provide an estimate of the half-life for these outer LMC clusters. As for the older clusters, they may result from processes taking place during the early evolution of the host. A problem of this scenario is that the metallicity predicted for clusters in the aforementioned simulations (where clusters formed from gas clouds pre-enriched by the formation of field stars) is higher than for LMC field stars, which is in disagreement with the results presented here. This discrepancy may be attenuated considering an inefficient gas mixing at the LMC outskirts.

Other photometric surveys are currently focused on the Magellanic Clouds, such as the Vista Magellanic Survey (Cioni & the VMC team 2015) and the Survey of the Magellanic Stellar History (Nidever & Smash Team 2015). Merging these data sets should result in a more complete picture of the Magellanic star clusters system and outer stellar populations. As these more remote regions should be strongly affected by the gravitational interaction involving the Galaxy, the LMC, the SMC and other dwarf galaxies sharing similar orbits and location, these combined surveys should be useful constraints to *N*-body simulations describing the origin and evolution of the Magellanic System.

ACKNOWLEDGEMENTS

We would like to thank the anonymous referee for many useful suggestions. This paper has gone through internal review by the DES collaboration.

AdP acknowledges financial support from the Brazilian Institution CNPq. EdB acknowledges financial support from the European Research Council (ERC-StG-335936, CLUSTERS).

We are grateful for the extraordinary contributions of our CTIO colleagues and the DECam Construction, Commissioning and Science Verification teams in achieving the excellent instrument and telescope conditions that have made this work possible. The success of this project also relies critically on the expertise and dedication of the DES Data Management group.

Funding for the DES Projects has been provided by the US Department of Energy, the US National Science Foundation, the Ministry of Science and Education of Spain, the Science and Technology Facilities Council of the United Kingdom, the Higher Education Funding Council for England, the National Center for Supercomputing Applications at the University of Illinois at Urbana-Champaign, the Kavli Institute of Cosmological Physics at the University of Chicago, the Center for Cosmology and Astro-Particle Physics at the Ohio State University, the Mitchell Institute for Fundamental Physics and Astronomy at Texas A&M University, Financiadora de Estudos e Projetos, Fundação Carlos Chagas Filho de Amparo à Pesquisa do Estado do Rio de Janeiro, Conselho Nacional de Desenvolvimento Científico e Tecnológico and the Ministério da Ciência, Tecnologia e Inovação, the Deutsche Forschungsgemeinschaft and the Collaborating Institutions in the Dark Energy Survey.

The Collaborating Institutions are Argonne National Laboratory, the University of California at Santa Cruz, the University of Cambridge, Centro de Investigaciones Enérgeticas, Medioambientales y Tecnológicas-Madrid, the University of Chicago, University College London, the DES-Brazil Consortium, the University of Edinburgh, the Eidgenössische Technische Hochschule (ETH) Zürich, Fermi National Accelerator Laboratory, the University of Illinois at Urbana-Champaign, the Institut de Ciències de l'Espai (IEEC/CSIC), the Institut de Física d'Altes Energies, Lawrence Berkeley National Laboratory, the Ludwig-Maximilians Universität München and the associated Excellence Cluster Universe, the University of Michigan, the National Optical Astronomy Observatory, the University of Nottingham, The Ohio State University, the University of Pennsylvania, the University of Portsmouth, SLAC National Accelerator Laboratory, Stanford University, the University of Sussex and Texas A&M University.

The DES data management system is supported by the National Science Foundation under Grant Number AST-1138766. The DES participants from Spanish institutions are partially supported by MINECO under grants AYA2012-39559, ESP2013-48274, FPA2013-47986 and Centro de Excelencia Severo Ochoa SEV-2012-0234. Research leading to these results has received funding from the European Research Council under the European Union's Seventh Framework Programme (FP7/2007-2013) including ERC grant agreements 240672, 291329 and 306478.

REFERENCES

Alves D. R., Nelson C. A., 2000, ApJ, 542, 789
Annunziatella M., Mercurio A., Brescia M., Cavuoti S., Longo G., 2013, PASP, 125, 68
Ashman K. M., Bird C. M., Zepf S. E., 1994, AJ, 108, 2348
Balbinot E., Santiago B. X., Girardi L., da Costa L. N., Maia M. A. G., Pellegrini P. S. S., Makler M., 2012, in Ballester P., Egret D., Lorente N. P. F., eds, ASP Conf. Ser. Vol. 461, Astronomical Data Analysis Software and Systems XXI. Astron. Soc. Pac., San Francisco, p. 287
Balbinot E. et al., 2015, MNRAS, 449, 1129
Bekki K., Chiba M., 2005, MNRAS, 356, 680
Bertin E., 2011, in Evans I. N., Accomazzi A., Mink D. J., Rots A. H., eds, ASP Conf. Ser. Vol. 442, Astronomical Data Analysis Software and Systems XX. Astron. Soc. Pac., San Francisco, p. 435
Bertin E., Arnouts S., 1996, A&AS, 117, 393
Bica E., Bonatto C., Dutra C. M., Santos J. F. C., 2008, MNRAS, 389, 678
Bressan A., Marigo P., Girardi L., Salasnich B., Dal Cero C., Rubele S., Nanni A., 2012, MNRAS, 427, 127
Caldwell J. A. R., Coulson I. M., 1986, MNRAS, 218, 223
Cardelli J. A., Clayton G. C., Mathis J. S., 1989, ApJ, 345, 245
Carrera R., Gallart C., Hardy E., Aparicio A., Zinn R., 2008, AJ, 135, 836
Carrera R., Gallart C., Aparicio A., Hardy E., 2011, AJ, 142, 61
Cioni M.-R. L., the VMC team 2015, preprint (arXiv:1503.06972)
de Grijs R., Wicker J. E., Bono G., 2014, AJ, 147, 122
Desai S. et al., 2012, ApJ, 757, 83
Elson R. A., Fall S. M., 1988, AJ, 96, 1383
Fisher R. A., 1956, Statistical Methods and Scientific Inference. Oliver and Boyd, Edinburgh, UK
Flaugher B. et al., 2015, AJ, 150, 150
Geisler D., Bica E., Dottori H., Claria J. J., Piatti A. E., Santos J. F. C., Jr, 1997, AJ, 114, 1920
Geisler D., Grocholski A. J., Sarajedini A., Cole A. A., Smith V. V., 2007, in Combes F., Palous J., eds, Proc. IAU Symp. 235, Galaxy Evolution Across the Hubble Time. Cambridge Univ. Press, Cambridge, p. 92
Girardi L., Chiosi C., Bertelli G., Bressan A., 1995, A&A, 298, 87
Girardi L., Bertelli G., Bressan A., Chiosi C., Groenewegen M. A. T., Marigo P., Salasnich B., Weiss A., 2002, A&A, 391, 195
Glatt K., Grebel E. K., Koch A., 2010, A&A, 517, AA50
Gordon K. D., Clayton G. C., Misselt K. A., Landolt A. U., Wolff M. J., 2003, ApJ, 594, 279
Grocholski A. J., Sarajedini A., Olsen K. A. G., Tiede G. P., Mancone C. L., 2007, AJ, 134, 680
Harris J., Zaritsky D., 2009, AJ, 138, 1243
Indu G., Subramaniam A., 2011, A&A, 535, A115
Kallivayalil N., van der Marel R. P., Besla G., Anderson J., Alcock C., 2013, ApJ, 764, 161
Kerber L. O., Santiago B. X., 2005, A&A, 435, 77
Kerber L. O., Santiago B. X., 2006, A&A, 452, 155
Kerber L. O., Santiago B. X., Brocato E., 2007, A&A, 462, 139
Kharchenko N. V., Piskunov A. E., Schilbach E., Röser S., Scholz R.-D., 2012, A&A, 543, A156
King I., 1962, ApJ, 67, 471
Kontizas M., Kontizas E., Michalitsianos A. G., 1993, A&A, 269, 107
Kroupa P., 2001, MNRAS, 322, 231
Kroupa P., Bastian U., 1997, New Astron., 2, 77
Kuehn C. A. et al., 2013, AJ, 145, 160
Lejeune T., Schaerer D., 2001, A&A, 366, 538
Leonardi A. J., Rose J. A., 2003, AJ, 126, 1811
Li C., de Grijs R., Deng L., 2014, ApJ, 784, 157
Livanou E., Dapergolas A., Kontizas M., Nordström B., Kontizas E., Andersen J., Dirsch B., Karampelas A., 2013, A&A, 554, A16
Lupton R., 1993, Statistics in Theory and Practice. Princeton Univ. Press, Princeton, NJ
Mackey A. D., Gilmore G. F., 2003, MNRAS, 338, 85
Martin N. F., de Jong J. T. A., Rix H.-W., 2008, ApJ, 684, 1075
Meschin I., Gallart C., Aparicio A., Hidalgo S. L., Monelli M., Stetson P. B., Carrera R., 2014, MNRAS, 438, 1067
Miocchi P. et al., 2013, ApJ, 774, 151
Mohr J. J. et al., 2012, in Radziwill N. M., Chiozzi G., eds, Proc. SPIE Conf. Ser. Vol. 8451, Software and Cyberinfrastructure for Astronomy II. SPIE, Bellingham, p. 84510D
Nemec J., Nemec A. F. L., 1991, PASP, 103, 95
Nidever D., Smash Team 2015, in Points S., Kunder A., eds, ASP Conf. Ser. Vol. 491, Fifty Years of Wide Field Studies in the Southern Hemisphere: Resolved Stellar Populations of the Galactic Bulge and Magellanic Clouds. Astron. Soc. Pac., San Francisco, p. 325
Nikolaev S., Drake A. J., Keller S. C., Cook K. H., Dalal N., Griest K., Welch D. L., Kanbur S. M., 2004, ApJ, 601, 260
Olsen K. A. G., Salyk C., 2002, AJ, 124, 2045
Olszewski E. W., Schommer R. A., Suntzeff N. B., Harris H. C., 1991, AJ, 101, 515
Pagel B. E. J., Tautvaisiene G., 1998, MNRAS, 299, 535
Palma T., Clariá J. J., Geisler D., Gramajo L. V., Ahumada A. V., 2015, MNRAS, 450, 2122
Piatti A. E., Geisler D., 2013, AJ, 145, 17
Piatti A. E., Keller S. C., Mackey A. D., Da Costa G. S., 2013, Bol. Asoc. Argentina Astron., 56, 275
Piatti A. E., Keller S. C., Mackey A. D., Da Costa G. S., 2014, MNRAS, 444, 1425
Schlegel D. J., Finkbeiner D. P., Davis M., 1998, ApJ, 500, 525
Sprott D. A., 2000, Statistical Inference in Science. Springer, Berlin,
Stetson P. B., 1987, PASP, 99, 191
Subramanian S., Subramaniam A., 2010, A&A, 520, A24
The Dark Energy Survey Collaboration 2005, preprint (astro-ph/0510346)
Weinberg M. D., Nikolaev S., 2001, ApJ, 548, 712
Weisz D. R., Dolphin A. E., Skillman E. D., Holtzman J., Dalcanton J. J., Cole A. A., Neary K., 2013, MNRAS, 431, 364
Werchan F., Zaritsky D., 2011, AJ, 142, 48

APPENDIX A: CLUSTERS LIST

We append the list of clusters for which we fit profiles and isochrones. We match cluster centroids (columns 2 and 3) to Bica et al. (2008) within a radius of 1 arcmin. The name of the nearest match is listed in column (1). In the case there are more than one object in the match, we assigned the nearest object. Columns (4) and (5) are the King profile core and tidal radius. Concentration [$c = \log(r_t/r_c)$] is listed in column (6). The age, metallicity, reddening and distance modulus are listed in the remaining columns, along with their associated uncertainties (for a 68 per cent confidence level).

Cluster name	α_c	δ_c	r_c(arcmin)	r_t(arcmin)	c	Age(Gyr)	Fe/H	$E(g-r)$	$m-M_0$
Reticulum cluster	69.042 30	−58.859 67	1.94 ± 0.01	3.40 ± 0.01	0.24	12.59 ± 0.29	−1.88 ± 0.12	0.00 ± 0.01	18.49 ± 0.01
SL126,ESO85SC21,KMHK322	74.342 42	−62.535 62	0.31 ± 0.02	1.31 ± 0.35	0.63	2.63 ± 0.06	−0.58 ± 0.06	0.00 ± 0.01	18.53 ± 0.01
DES001SC01	75.818 22	−64.029 76	0.18 ± 0.03	0.72 ± 0.73	0.59	2.82 ± 0.13	−0.88 ± 0.12	0.04 ± 0.02	18.32 ± 0.05
SL214,LW130,ESO85SC41,KMHK512	76.351 51	−63.287 54	0.50 ± 0.05	0.75 ± 0.48	0.17	1.20 ± 0.03	−0.88 ± 0.12	0.10 ± 0.01	18.12 ± 0.01
SL233,ESO85SC45,KMHK543	76.766 07	−63.647 70	0.42 ± 0.03	0.99 ± 0.28	0.37	2.57 ± 0.06	−0.70 ± 0.09	0.00 ± 0.02	18.14 ± 0.04
SL262,LW146,ESO119SC40,KMHK582	77.340 28	−62.379 69	0.56 ± 0.03	1.49 ± 0.23	0.42	2.63 ± 0.06	−0.70 ± 0.08	0.01 ± 0.01	18.45 ± 0.01
SL273,KMHK597	77.474 75	−63.638 29	0.36 ± 0.03	0.61 ± 0.34	0.23	1.58 ± 0.07	−0.58 ± 0.06	0.00 ± 0.01	18.42 ± 0.02
DES001SC02	77.709 62	−64.528 80	0.42 ± 0.10	1.24 ± 0.34	0.47	0.87 ± 0.64	−1.18 ± 0.10	0.08 ± 0.01	18.09 ± 0.16
BSDL818	77.925 11	−64.653 23	0.17 ± 0.07	0.74 ± 0.80	0.64	0.72 ± 0.25	−0.23 ± 0.14	0.00 ± 0.10	18.73 ± 0.18
SL303,LW158,KMHK644	78.085 93	−64.303 82	0.36 ± 0.05	3.67 ± 0.17	1.01	2.63 ± 0.06	−0.58 ± 0.08	0.00 ± 0.01	18.62 ± 0.04
DES001SC03	78.102 03	−64.027 77	0.27 ± 0.06	0.65 ± 0.52	0.38	0.83 ± 0.06	−0.58 ± 0.06	0.13 ± 0.01	18.11 ± 0.13
NGC1868,SL330,LW169,ESO85SC56,	78.652 51	−63.957 14	1.65 ± 0.01	2.35 ± 0.01	0.15	1.26 ± 0.03	−0.88 ± 0.12	0.09 ± 0.02	18.35 ± 0.01
ESO119SC50,KMHK705	79.173 49	−62.023 92	0.12 ± 0.02	1.10 ± 0.60	0.94	1.45 ± 0.03	−0.28 ± 0.05	0.05 ± 0.01	18.34 ± 0.04
SL354,LW177,ESO85SC63,KMHK712	79.384 39	−63.420 73	0.89 ± 0.08	1.79 ± 0.12	0.30	2.63 ± 0.06	−0.58 ± 0.06	0.01 ± 0.01	18.39 ± 0.01
H88-257,H80F4-6	79.453 94	−64.044 71	0.22 ± 0.05	0.75 ± 0.53	0.52	2.63 ± 0.61	−0.70 ± 0.25	0.05 ± 0.03	18.25 ± 0.01
H88-258,H80F4-7,KMHK720	79.465 27	−63.795 10	0.39 ± 0.05	0.71 ± 0.48	0.26	1.05 ± 0.07	−0.88 ± 0.12	0.14 ± 0.01	17.99 ± 0.07
SL372,LW180,KMHK730	79.659 56	−64.112 18	0.71 ± 0.13	1.06 ± 0.46	0.17	1.35 ± 0.06	−0.70 ± 0.11	0.08 ± 0.06	17.90 ± 0.02
NGC1900,SL376,LW184,ESO85SC68,	79.740 75	−63.024 12	0.49 ± 0.05	1.30 ± 0.04	0.43	1.32 ± 0.09	−1.18 ± 0.11	0.10 ± 0.01	17.97 ± 0.01
SL388,LW186,ESO85SC72,KMHK773	80.023 39	−63.480 33	0.54 ± 0.03	2.55 ± 0.14	0.68	2.57 ± 0.06	−0.58 ± 0.06	0.00 ± 0.01	18.61 ± 0.02
OHSC10,KMHK782	80.162 00	−63.135 00	0.17 ± 0.04	1.30 ± 0.56	0.89	1.20 ± 0.03	−1.18 ± 0.20	0.13 ± 0.01	17.99 ± 0.01
SL401,LW190,KMHK791	80.209 39	−64.003 91	0.28 ± 0.03	1.74 ± 0.36	0.80	2.40 ± 0.06	−0.70 ± 0.08	0.07 ± 0.01	18.27 ± 0.03
KMHK815	80.492 40	−64.598 99	0.35 ± 0.06	0.36 ± 0.14	0.02	0.87 ± 0.08	−0.28 ± 0.08	0.01 ± 0.02	18.46 ± 0.15
LW195,ESO119SC61,KMHK821	80.647 59	−61.879 43	0.33 ± 0.03	1.59 ± 0.32	0.68	1.95 ± 0.05	−0.48 ± 0.07	0.01 ± 0.01	18.48 ± 0.09
DES001SC04	81.132 15	−64.325 42	0.12 ± 0.04	0.47 ± 0.26	0.61	4.17 ± 1.08	−0.88 ± 0.12	0.06 ± 0.05	18.37 ± 0.10
KMHK854	81.170 56	−63.203 52	0.12 ± 0.04	1.46 ± 0.60	1.07	1.29 ± 0.16	−1.18 ± 0.11	0.15 ± 0.02	17.90 ± 0.12
NGC1942,SL445,LW203,ESO85SC81,	81.179 74	−63.939 37	0.80 ± 0.06	1.69 ± 0.23	0.32	1.41 ± 0.03	−0.88 ± 0.16	0.06 ± 0.01	18.60 ± 0.01
SL448,LW205,ESO85SC82,KMHK859	81.248 78	−63.048 50	0.28 ± 0.04	1.16 ± 0.38	0.62	2.45 ± 0.06	−0.88 ± 0.12	0.02 ± 0.01	18.22 ± 0.01
LW208,KMHK878	81.394 92	−64.758 10	0.08 ± 0.01	2.70 ± 0.53	1.52	0.72 ± 0.15	−0.48 ± 0.10	0.06 ± 0.02	18.35 ± 0.01
LW212,KMHK882,BSDL1630	81.537 31	−64.565 97	0.48 ± 0.07	1.33 ± 0.28	0.44	1.26 ± 0.19	−0.88 ± 0.30	0.19 ± 0.01	18.27 ± 0.14
BSDL1735	81.816 36	−64.261 48	0.16 ± 0.04	2.77 ± 0.45	1.25	0.69 ± 0.02	−0.28 ± 0.06	0.03 ± 0.02	18.59 ± 0.01
DES001SC05	81.921 98	−64.807 29	0.16 ± 0.05	1.28 ± 0.88	0.91	0.76 ± 0.07	−0.40 ± 0.10	0.07 ± 0.04	18.59 ± 0.11
SL484,LW216,KMHK918	81.946 00	−64.649 97	0.24 ± 0.05	1.04 ± 0.54	0.64	0.34 ± 0.03	−0.23 ± 0.09	0.05 ± 0.01	18.47 ± 0.14
DES001SC08	81.973 49	−64.175 41	0.39 ± 0.02	0.39 ± 0.19	0.01	1.26 ± 0.40	−1.18 ± 0.10	0.10 ± 0.04	18.08 ± 0.12
KMHK938	82.182 39	−64.680 12	0.16 ± 0.03	1.83 ± 0.40	1.06	1.00 ± 0.26	−0.40 ± 0.07	0.08 ± 0.04	18.38 ± 0.16
DES001SC07	82.188 70	−64.058 64	0.22 ± 0.06	1.29 ± 0.48	0.77	1.41 ± 0.10	−0.88 ± 0.12	0.11 ± 0.04	18.21 ± 0.08
HS317,KMHK947	82.254 36	−64.288 81	0.12 ± 0.04	1.51 ± 0.70	1.12	0.30 ± 0.04	−0.18 ± 0.03	0.07 ± 0.05	18.51 ± 0.01

Cluster name	α_c	δ_c	r_c(arcmin)	r_t(arcmin)	c	Age(Gyr)	Fe/H	$E(g-r)$	$m-M_0$
DES001SC06	82.371 92	−63.083 30	0.46 ± 0.01	0.48 ± 0.32	0.01	1.82 ± 0.04	−0.48 ± 0.10	0.05 ± 0.01	18.43 ± 0.04
SL509,LW221,ESO85SC91,KMHK957	82.450 45	−63.649 79	0.88 ± 0.07	1.59 ± 0.12	0.25	1.26 ± 0.03	−1.18 ± 0.09	0.15 ± 0.01	18.26 ± 0.02
SL511,LW222,KMHK959	82.453 66	−64.438 82	0.26 ± 0.07	3.29 ± 0.37	1.10	2.00 ± 0.09	−0.70 ± 0.08	0.10 ± 0.01	18.14 ± 0.01
SL515,LW223,ESO85SC92,KMHK965	82.534 06	−63.426 85	0.55 ± 0.05	2.15 ± 0.19	0.59	1.26 ± 0.03	−0.88 ± 0.12	0.08 ± 0.01	18.43 ± 0.01
SL525,LW225,KMHK973	82.593 68	−64.017 76	0.47 ± 0.02	0.49 ± 0.40	0.03	2.88 ± 1.10	−0.88 ± 0.13	0.01 ± 0.03	18.30 ± 0.02
NGC1997,SL520,LW226,ESO86SC1,	82.643 48	−63.204 79	0.85 ± 0.05	1.79 ± 0.20	0.33	4.47 ± 0.10	−1.18 ± 0.09	0.08 ± 0.01	18.33 ± 0.01
SL529,LW229,ESO86SC5,KMHK992	82.780 57	−63.540 49	0.41 ± 0.05	2.31 ± 0.23	0.76	2.88 ± 0.07	−0.88 ± 0.12	0.01 ± 0.01	18.47 ± 0.02
OHSC20	82.833 36	−63.670 46	0.18 ± 0.03	0.96 ± 0.63	0.71	3.80 ± 0.37	−1.18 ± 0.09	0.08 ± 0.07	18.28 ± 0.06
LW230	82.847 62	−63.261 48	0.30 ± 0.04	0.66 ± 0.48	0.35	0.06 ± 0.07	−0.18 ± 0.06	0.15 ± 0.04	18.00 ± 0.16
DES001SC10	82.856 39	−63.453 56	0.27 ± 0.04	0.50 ± 0.44	0.27	1.51 ± 0.15	−1.18 ± 0.09	0.17 ± 0.06	18.32 ± 0.16
SL540,LW232,KMHK1003	82.893 60	−63.887 14	0.16 ± 0.04	2.19 ± 0.51	1.13	0.93 ± 0.07	−0.88 ± 0.12	0.10 ± 0.01	18.24 ± 0.19
DES001SC09	82.956 84	−63.322 52	0.32 ± 0.07	0.84 ± 0.56	0.42	1.20 ± 0.18	−0.88 ± 0.12	0.09 ± 0.03	18.31 ± 0.10
H4,SL556,LW237,ESO86SC9,KMHK1034	83.107 91	−64.736 54	0.83 ± 0.05	3.44 ± 0.03	0.62	2.34 ± 0.11	−0.88 ± 0.12	0.01 ± 0.02	18.70 ± 0.02
DES001SC12	83.340 19	−63.596 30	0.12 ± 0.05	1.43 ± 0.76	1.06	2.40 ± 0.62	−0.70 ± 0.34	0.02 ± 0.04	18.39 ± 0.04
DES001SC13	83.404 47	−63.071 90	0.12 ± 0.03	2.36 ± 0.73	1.28	1.32 ± 0.16	−0.34 ± 0.10	0.00 ± 0.06	18.37 ± 0.10
DES001SC16	83.701 46	−62.422 95	0.34 ± 0.06	1.15 ± 0.76	0.53	1.38 ± 0.32	−0.88 ± 0.30	0.16 ± 0.01	18.10 ± 0.20
OHSC22,KMHK1089	83.714 19	−63.632 54	0.23 ± 0.03	0.61 ± 0.66	0.43	0.44 ± 0.27	−0.58 ± 0.23	0.06 ± 0.03	18.35 ± 0.20
DES001SC11	83.770 45	−63.538 94	0.08 ± 0.03	0.52 ± 0.66	0.79	0.95 ± 0.09	−0.70 ± 0.09	0.09 ± 0.02	18.26 ± 0.02
DES001SC14	83.803 42	−64.618 81	0.12 ± 0.05	0.47 ± 0.89	0.61	0.76 ± 1.10	−0.34 ± 0.06	0.02 ± 0.06	18.49 ± 0.18
E2,ESO120SC08,KMHK1119	84.090 11	−61.788 61	0.46 ± 0.04	1.74 ± 0.32	0.58	2.24 ± 0.05	−0.88 ± 0.12	0.10 ± 0.01	18.17 ± 0.01
LW250,KMHK1129	84.158 28	−64.386 28	0.37 ± 0.04	0.97 ± 0.40	0.42	0.98 ± 0.05	−0.70 ± 0.08	0.02 ± 0.01	18.43 ± 0.01
SL604,LW251,KMHK1127	84.192 08	−62.884 30	0.42 ± 0.03	0.99 ± 0.30	0.37	2.63 ± 0.06	−0.70 ± 0.08	0.01 ± 0.01	18.43 ± 0.01
DES001SC15	84.572 19	−64.505 97	0.67 ± 0.17	0.68 ± 0.34	0.00	2.63 ± 3.83	−0.88 ± 0.44	0.10 ± 0.06	18.27 ± 0.18
LW260,KMHK1168	84.721 74	−64.292 17	0.16 ± 0.07	0.65 ± 0.69	0.62	0.44 ± 0.09	−0.48 ± 0.20	0.04 ± 0.04	18.35 ± 0.12
DES001SC17	84.745 72	−62.456 73	0.32 ± 0.01	0.33 ± 0.36	0.01	1.26 ± 0.36	−0.48 ± 0.21	0.02 ± 0.09	18.33 ± 0.02
DES001SC20	84.798 94	−62.585 97	0.39 ± 0.08	3.07 ± 0.55	0.89	1.45 ± 0.03	−0.88 ± 0.12	0.10 ± 0.01	18.32 ± 0.02
KMHK1195	85.096 80	−64.248 33	0.61 ± 0.02	0.62 ± 0.31	0.00	1.26 ± 0.12	−0.18 ± 0.09	0.00 ± 0.04	18.40 ± 0.10
LW266,KMHK1198	85.131 32	−64.298 48	0.20 ± 0.08	2.12 ± 0.70	1.02	0.69 ± 0.10	−0.48 ± 0.10	0.03 ± 0.03	18.53 ± 0.10
DES001SC19	85.144 43	−63.100 33	0.15 ± 0.03	0.35 ± 0.21	0.37	1.41 ± 0.21	−0.88 ± 0.26	0.08 ± 0.08	18.18 ± 0.01
DES001SC18	85.172 62	−63.818 72	0.13 ± 0.05	0.53 ± 0.49	0.62	1.32 ± 0.30	−0.88 ± 0.25	0.12 ± 0.01	18.15 ± 0.06
SL649,LW269,KMHK1214	85.288 48	−63.771 32	0.31 ± 0.04	2.11 ± 0.33	0.83	2.45 ± 0.12	−0.88 ± 0.12	0.03 ± 0.02	18.60 ± 0.02
BSDL2771	85.366 40	−63.132 42	0.32 ± 0.14	1.12 ± 0.75	0.55	1.26 ± 0.19	−0.88 ± 0.20	0.10 ± 0.08	18.11 ± 0.01
DES001SC22	85.474 93	−62.361 56	0.13 ± 0.03	1.44 ± 0.74	1.03	2.29 ± 0.40	−0.58 ± 0.25	0.00 ± 0.06	18.57 ± 0.18
LW272,KMHK1241	85.607 24	−62.501 70	0.14 ± 0.05	3.08 ± 0.63	1.33	2.09 ± 0.10	−0.88 ± 0.12	0.10 ± 0.01	18.32 ± 0.05
DES001SC21	85.764 33	−62.528 62	0.20 ± 0.06	1.01 ± 0.58	0.70	2.51 ± 0.06	−0.70 ± 0.08	0.05 ± 0.02	18.35 ± 0.09
LW276,KMHK1269	85.801 17	−63.617 29	0.50 ± 0.01	0.51 ± 0.22	0.00	2.88 ± 0.07	−0.88 ± 0.12	0.01 ± 0.01	18.45 ± 0.03
LW278,KMHK1265	85.801 60	−62.470 70	0.26 ± 0.03	0.79 ± 0.53	0.49	2.63 ± 0.06	−0.88 ± 0.12	0.06 ± 0.01	18.36 ± 0.01
SL670,LW277,ESO86SC25,KMHK1268	85.808 29	−62.833 91	0.33 ± 0.02	1.59 ± 0.29	0.68	2.57 ± 0.06	−0.58 ± 0.06	0.01 ± 0.01	18.55 ± 0.02
KMHK1278	85.868 77	−63.414 79	0.13 ± 0.04	2.02 ± 0.59	1.20	1.38 ± 0.28	−0.88 ± 0.12	0.10 ± 0.02	18.03 ± 0.12
SL677,LW280,KMHK1286	85.981 55	−63.373 42	0.29 ± 0.04	0.86 ± 0.44	0.47	0.65 ± 0.05	−0.88 ± 0.20	0.00 ± 0.02	18.50 ± 0.01
SL680,LW281,KMHK1290	86.017 61	−63.924 66	0.31 ± 0.12	3.07 ± 0.37	0.99	0.63 ± 0.05	−0.23 ± 0.11	0.01 ± 0.03	18.45 ± 0.11

Cluster name	α_c	δ_c	r_c(arcmin)	r_t(arcmin)	c	Age(Gyr)	Fe/H	$E(g-r)$	$m-M_0$
NGC2097,SL682,LW282,ESO56SC28,	86.029 48	−62.783 51	0.85 ± 0.02	1.61 ± 0.02	0.28	1.10 ± 0.03	−0.88 ± 0.12	0.08 ± 0.01	18.37 ± 0.01
SL689,LW284,KMHK1310	86.142 88	−65.001 71	0.23 ± 0.08	0.84 ± 0.34	0.56	1.02 ± 0.02	−0.70 ± 0.08	0.18 ± 0.01	18.13 ± 0.01
SL694,LW287,KMHK1318	86.278 04	−63.676 21	0.21 ± 0.03	0.40 ± 0.09	0.27	1.20 ± 0.06	−0.28 ± 0.06	0.02 ± 0.02	18.67 ± 0.04
KMHK1322	86.288 98	−64.797 39	0.20 ± 0.05	1.22 ± 0.50	0.80	1.58 ± 0.23	−0.58 ± 0.27	0.01 ± 0.05	18.52 ± 0.08
SL696,LW286,KMHK1324	86.312 40	−64.772 44	0.19 ± 0.04	0.69 ± 0.51	0.57	1.12 ± 0.03	−0.88 ± 0.12	0.11 ± 0.01	18.13 ± 0.02
SL701,LW289,ESO56SC30,KMHK1330	86.391 15	−63.715 73	0.43 ± 0.06	3.29 ± 0.28	0.89	1.38 ± 0.03	−0.70 ± 0.08	0.06 ± 0.01	18.10 ± 0.06
BSDL2976	86.743 97	−63.863 92	0.80 ± 0.08	1.86 ± 0.17	0.37	0.48 ± 0.01	−0.23 ± 0.03	0.02 ± 0.01	18.27 ± 0.02
OHSC26	86.848 54	−62.622 15	0.11 ± 0.04	0.54 ± 0.30	0.68	0.89 ± 0.06	−0.40 ± 0.07	0.00 ± 0.07	18.55 ± 0.01
SL720,LW299,KMHK1373	86.945 25	−65.011 15	0.44 ± 0.02	0.64 ± 0.36	0.16	2.04 ± 0.15	−0.58 ± 0.10	0.05 ± 0.07	18.41 ± 0.01
KMHK1381	87.038 43	−63.598 45	0.23 ± 0.03	0.93 ± 0.06	0.60	1.15 ± 0.03	−0.70 ± 0.08	0.08 ± 0.01	18.11 ± 0.02
DES001SC23	87.196 62	−65.152 52	0.33 ± 0.07	1.13 ± 0.22	0.54	0.35 ± 0.01	−0.01 ± 0.01	0.02 ± 0.01	18.58 ± 0.01
SL724,LW305,KMHK1388	87.222 06	−64.633 12	0.24 ± 0.04	0.94 ± 0.35	0.60	1.10 ± 0.08	−0.48 ± 0.20	0.03 ± 0.04	18.33 ± 0.18
SL726,LW306,KMHK1390	87.245 26	−64.733 59	0.34 ± 0.04	0.69 ± 0.41	0.31	1.00 ± 0.32	−0.40 ± 0.10	0.00 ± 0.06	18.40 ± 0.13
KMHK1391	87.258 21	−64.348 38	0.55 ± 0.02	0.57 ± 0.35	0.01	1.51 ± 0.18	−0.70 ± 0.10	0.07 ± 0.02	18.37 ± 0.04
SL727,LW307,KMHK1393	87.260 73	−65.012 12	0.35 ± 0.05	2.63 ± 0.20	0.88	1.82 ± 0.04	−0.88 ± 0.12	0.01 ± 0.01	18.57 ± 0.01
SL729,LW311,KMHK1399	87.334 53	−63.134 70	0.38 ± 0.06	1.42 ± 0.48	0.57	1.10 ± 0.03	−0.40 ± 0.10	0.02 ± 0.01	18.50 ± 0.01
SL738,LW314,KMHK1417	87.533 06	−64.153 52	0.21 ± 0.05	2.58 ± 0.33	1.09	1.29 ± 0.12	−0.70 ± 0.13	0.05 ± 0.03	18.42 ± 0.01
NGC2120,SL742,LW316,ESO86SC34,	87.645 99	−63.675 48	1.07 ± 0.03	2.17 ± 0.02	0.31	1.78 ± 0.04	−0.58 ± 0.06	0.00 ± 0.01	18.50 ± 0.01
LW319,KMHK1439	87.772 90	−64.187 43	0.44 ± 0.02	0.47 ± 0.14	0.03	1.10 ± 0.05	−0.70 ± 0.08	0.06 ± 0.01	18.10 ± 0.03
LW320,KMHK1447	87.840 75	−62.992 15	0.31 ± 0.03	1.39 ± 0.30	0.66	3.02 ± 0.14	−1.18 ± 0.10	0.07 ± 0.01	18.27 ± 0.01
LW323,KMHK1455	87.938 22	−63.865 62	0.59 ± 0.07	0.87 ± 0.40	0.17	1.91 ± 0.04	−0.58 ± 0.06	0.00 ± 0.01	18.36 ± 0.01
OHSC27,KMHK1469	88.122 57	−63.600 65	0.70 ± 0.06	0.79 ± 0.38	0.05	1.32 ± 0.20	−0.88 ± 0.35	0.05 ± 0.08	18.21 ± 0.20
KMHK1484	88.298 43	−63.806 91	0.48 ± 0.03	0.49 ± 0.30	0.00	0.83 ± 0.29	−0.40 ± 0.16	0.02 ± 0.10	18.47 ± 0.16
SL768,LW326,ESO86SC38,KMHK1493	88.473 78	−63.615 44	0.68 ± 0.05	3.62 ± 0.05	0.72	1.51 ± 0.04	−0.34 ± 0.03	0.00 ± 0.01	18.40 ± 0.01
DES001SC26	88.559 20	−65.147 52	0.31 ± 0.09	0.79 ± 0.49	0.41	1.35 ± 0.10	−0.88 ± 0.17	0.08 ± 0.05	18.16 ± 0.10
DES001SC25	88.654 18	−64.887 16	0.11 ± 0.04	1.12 ± 0.75	1.02	0.81 ± 0.08	−0.28 ± 0.12	0.02 ± 0.04	18.48 ± 0.14
LW332,KMHK1518	88.778 51	−64.652 82	0.33 ± 0.10	0.83 ± 0.48	0.40	1.00 ± 0.07	−0.88 ± 0.12	0.11 ± 0.02	18.41 ± 0.01
OHSC28	88.897 00	−62.345 24	0.29 ± 0.01	0.38 ± 0.12	0.13	2.63 ± 0.32	−0.58 ± 0.06	0.05 ± 0.01	18.38 ± 0.01
BSDL3181	88.970 86	−65.293 11	0.38 ± 0.06	0.73 ± 0.56	0.28	0.83 ± 0.04	−1.18 ± 0.11	0.14 ± 0.04	18.39 ± 0.02
KMHK1530	89.034 12	−63.642 78	0.17 ± 0.06	1.58 ± 0.57	0.97	2.63 ± 0.06	−0.88 ± 0.12	0.06 ± 0.01	18.50 ± 0.01
DES001SC24	89.082 72	−64.717 55	0.17 ± 0.06	1.18 ± 0.57	0.84	1.26 ± 0.33	−1.18 ± 0.09	0.12 ± 0.01	18.31 ± 0.04
BSDL3189	89.384 47	−65.343 30	0.15 ± 0.04	1.29 ± 0.58	0.94	1.91 ± 0.04	−0.58 ± 0.06	0.06 ± 0.01	18.45 ± 0.01
LW340,KMHK1548	89.397 15	−64.998 39	0.34 ± 0.06	1.19 ± 0.49	0.55	2.51 ± 0.18	−0.88 ± 0.15	0.05 ± 0.05	18.41 ± 0.10
SL798,LW344,KMHK1556	89.550 14	−63.894 50	0.22 ± 0.05	1.22 ± 0.52	0.74	2.51 ± 0.31	−0.88 ± 0.12	0.06 ± 0.02	18.20 ± 0.10
DES001SC27	89.608 03	−64.594 79	0.10 ± 0.03	1.05 ± 0.67	1.03	1.10 ± 0.16	−0.70 ± 0.26	0.06 ± 0.07	18.10 ± 0.14
NGC2162,SL814,LW351,ESO86SC47,	90.125 89	−63.721 73	0.91 ± 0.03	1.86 ± 0.05	0.31	1.29 ± 0.03	−0.88 ± 0.12	0.08 ± 0.02	18.36 ± 0.01
KMHK1593	90.466 76	−64.132 92	0.14 ± 0.03	2.34 ± 0.49	1.23	3.39 ± 0.41	−0.88 ± 0.12	0.03 ± 0.03	18.33 ± 0.01
ESO121SC03,KMHK1591	90.513 84	−60.523 79	0.47 ± 0.04	2.63 ± 0.09	0.75	9.77 ± 0.23	−1.40 ± 0.05	0.07 ± 0.01	18.14 ± 0.01
DES001SC28	90.829 90	−64.831 38	0.15 ± 0.04	1.15 ± 0.64	0.89	0.79 ± 0.10	−0.70 ± 0.08	0.08 ± 0.02	18.83 ± 0.10
NGC2193,SL839,LW387,ESO86SC57	91.572 13	−65.098 74	0.46 ± 0.05	3.29 ± 0.26	0.85	2.40 ± 0.06	−0.70 ± 0.08	0.01 ± 0.01	18.47 ± 0.01

[1] *Instituto de Física, Universidade Federal do Rio Grande do Sul, Caixa Postal 15051, Porto Alegre, RS - 91501-970, Brazil*
[2] *Laboratório Interinstitucional de e-Astronomia - LIneA, Rua Gal. José Cristino 77, Rio de Janeiro, RJ - 20921-400, Brazil*
[3] *Department of Physics, University of Surrey, Guildford GU2 7XH, UK*
[4] *Observatório Nacional, Rua Gal. José Cristino 77, Rio de Janeiro, RJ - 20921-400, Brazil*
[5] *Fermi National Accelerator Laboratory, PO Box 500, Batavia, IL 60510, USA*
[6] *Kavli Institute for Particle Astrophysics and Cosmology, PO Box 2450, Stanford University, Stanford, CA 94305, USA*
[7] *SLAC National Accelerator Laboratory, Menlo Park, CA 94025, USA*
[8] *Cerro Tololo Inter-American Observatory, National Optical Astronomy Observatory, Casilla 603, La Serena, Chile*
[9] *CNRS, UMR 7095, Institut d'Astrophysique de Paris, F-75014 Paris, France*
[10] *Department of Physics and Astronomy, University College London, Gower Street, London WC1E 6BT, UK*
[11] *Sorbonne Universités, UPMC Univ Paris 06, UMR 7095, Institut d'Astrophysique de Paris, F-75014 Paris, France*
[12] *Department of Astronomy, University of Illinois, 1002 W. Green Street, Urbana, IL 61801, USA*
[13] *National Center for Supercomputing Applications, 1205 West Clark St, Urbana, IL 61801, USA*
[14] *Institut de Ciències de l'Espai, IEEC-CSIC, Campus UAB, Carrer de Can Magrans, s/n, E-08193 Bellaterra, Barcelona, Spain*
[15] *Institut de Física d'Altes Energies (IFAE), The Barcelona Institute of Science and Technology, Campus UAB, E-08193 Bellaterra, Barcelona, Spain*
[16] *Excellence Cluster Universe, Boltzmannstr. 2, D-85748 Garching, Germany*
[17] *Faculty of Physics, Ludwig-Maximilians University, Scheinerstr. 1, D-81679 Munich, Germany*
[18] *Jet Propulsion Laboratory, California Institute of Technology, 4800 Oak Grove Dr, Pasadena, CA 91109, USA*
[19] *Department of Physics, University of Michigan, Ann Arbor, MI 48109, USA*
[20] *Center for Cosmology and Astro-Particle Physics, The Ohio State University, Columbus, OH 43210, USA*
[21] *Department of Physics, The Ohio State University, Columbus, OH 43210, USA*
[22] *Australian Astronomical Observatory, North Ryde, NSW 2113, Australia*
[23] *George P. and Cynthia Woods Mitchell Institute for Fundamental Physics and Astronomy, and Department of Physics and Astronomy, Texas A&M University, College Station, TX 77843, USA*
[24] *Department of Astronomy, The Ohio State University, Columbus, OH 43210, USA*
[25] *Department of Astronomy, University of Michigan, Ann Arbor, MI 48109, USA*
[26] *Institució Catalana de Recerca i Estudis Avançats, E-08010 Barcelona, Spain*
[27] *Institute of Cosmology and Gravitation, University of Portsmouth, Portsmouth PO1 3FX, UK*
[28] *Department of Physics and Astronomy, Pevensey Building, University of Sussex, Brighton BN1 9QH, UK*
[29] *Centro de Investigaciones Energéticas, Medioambientales y Tecnológicas (CIEMAT), Madrid, Spain*
[30] *ICTP South American Institute for Fundamental Research Instituto de Física Teórica, Universidade Estadual Paulista, São Paulo, Brazil*
[31] *Department of Physics and Astronomy, University of Pennsylvania, Philadelphia, PA 19104, USA*
[32] *Department of Physics, University of Illinois, 1110 W. Green St, Urbana, IL 61801, USA*

This paper has been typeset from a TEX/LATEX file prepared by the author.